# Nano Scale Disruptive Silicon-Plasmonic Platform for Chip-to-Chip Interconnection

# Report on SPP amplifiers by using QDs

| | |
|---|---|
| Deliverable no.: | D4.4 |
| Due date: | 04/30/2014 |
| Actual Submission date: | 10/22/2014 |
| Authors: | IMEC, UVEG, UGent |
| Work package(s): | WP4 |
| Distribution level: | RE[1] (NAVOLCHI Consortium)<br>Nature: document, available online in the restricted area of the NAVOLCHI webpage |

## List of Partners concerned

| Partner number | Partner name | Partner short name | Country | Date enter project | Date exit project |
|---|---|---|---|---|---|
| 2 | INTERUNIVERSITAIR MICRO-ELECTRONICA CENTRUM VZW | IMEC | Belgium | M1 | M36 |
| 5 | UNIVERSITAT DE VALENCIA | UVEG | Spain | M1 | M36 |
| 7 | UNIVERSITEIT GENT | UGent | Belgium | M1 | M36 |

[1] **PU** = Public
**PP** = Restricted to other programme participants (including the Commission Services)
**RE** = Restricted to a group specified by the consortium (including the Commission Services)
**CO** = Confidential, only for members of the consortium (including the Commission Services)

### *Deliverable Responsible*

Organization: INTERUNIVERSITAIR MICRO-ELECTRONICA CENTRUM VZW (IMEC)
Contact Person: Dries Van Thourhout
Address: St. Pietersnieuwstraat 41
9000 Gent
Belgium
Phone: +32 9 264 3438
E-mail: dries.vanthourhout@imec.be

### *Executive Summary*

This report deals with the use of QD-PMMA nanocomposite to compensate losses in plasmonic waveguides. The studies have been carried out both on visible and infrared wavelengths (1400-1600 nm). Results at visible wavelengths are only included as a proof of concept and testing purposes by using CdSe QDs (available in more quantity and higher signal-to-noise ratio in photodetection). The report includes the two working designs of the plasmonic amplifiers by using optical pumping. The first one is regarding waveguides using QD-polymer nanocomposites as dielectric waveguides for the compensation of losses along the propagation of surface plasmon polaritons. The second design uses SiN-waveguides with embedded QDs. Applying an AC-field allows for electrical injection.

### *Change Records*

| Version | Date | Changes | Author |
|---|---|---|---|
| 0.1 | 2014-09-20 | First version | Isaac Suárez |
| 0.2 | 2014-09-30 | Second version | Juan Martínez Pastor |
| 0.3 | 2014-10-12 | Third version | Juan Martínez Pastor |

# *Contents*

# 1 Introduction and objectives

Surface plasmons (SP) are coherent oscillations of free electrons present at the boundary between a metal and a dielectric. Under appropriate conditions when SPs are exposed to a flow of visible or infrared light, such oscillations can be coupled to the incident photons leading to a hybrid electromagnetic-wave and surface-charge state known as surface plasmon polariton (SPP). In these conditions SPP can propagate along the interface showing unique properties as subwavelength confinement, strong near electromagnetic field enhancement or high sensitivity to the environment [1] which could be used to miniaturize the final size of the device and reduce its power consumption in future electronic/photonic technology [2]. However, the propagation length (LP) of SPPs is reduced by the high ohmic losses in metals to ten times the operation wavelength limiting the application of SPP's waveguides. Nevertheless, this limitation can be compensated by an appropriate design of the plasmonic waveguide. A first approach is to provide gain in the dielectric on top of the metal that could amplify the SPP signal [3]. In addition, the propagation length can be increased by combining the SPP with dielectric waveguide modes [4], which usually exhibit small propagation losses. In this work a combination of both solutions is presented as a method to couple light into the SPP and to increase its Lp.

The idea of obtaining a lossless propagation SPP by a gain assisted dielectric has been studied recently in long range SPP modes (LR-SPP) travelling in gold or silver plasmonic waveguides. These modes exist in insulator-metal-insulator (IMI) structures and are characterized by high field localization in the dielectric medium [5]. In this way, absorption losses can be compensated and the SPP propagation length significantly increased (see figure 1b). In the literature different materials like dyes [6], fluorescent polymers [7], rare earths [8] or PbSe quantum dots [9] have been proposed as gain medium for wavelengths between 600 and 1500 nm.

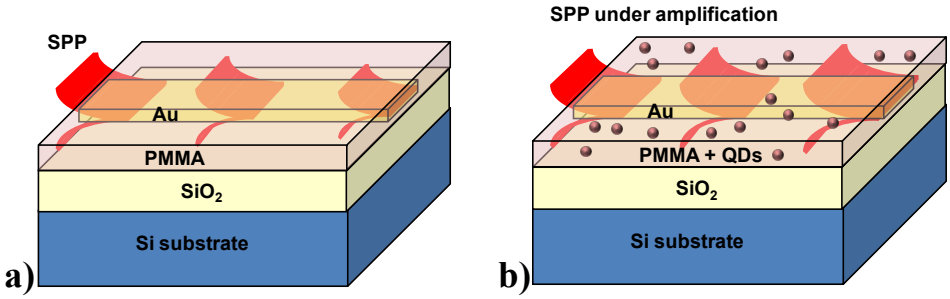


**Figure 1. Structure of the surface plasmon polariton waveguide and propagation without (a) and with amplification (b).**

In Navolchi this problem is proposed to be overcome by two different approaches based on colloidal quantum dots (QD) as a gain medium. These nanostructures are semiconductor nanocrystal synthetized by colloidal chemistry and have the advantages of a room temperature emission and color tuning with their size or the base material.

- In the first approach a novel material based on the incorporation of colloidal quantum dots in a polymer matrix is proposed as a dielectric medium to provide gain in plasmonic waveguides. This kind of nanocomposite (polymer+quantum dots) is useful, because it combines the novel properties of colloidal quantum dots with the technological feasibility of polymers (spin coating, UV and e-beam lithography). Indeed, the application of CdSe/PMMA in the development of active

dielectric waveguides has already been demonstrated at 600 nm [10-11] by depositing the nanocomposite on a $SiO_2$/Si substrate. Then, in the project it is proposed to deposit QD-PMMA (or QD-SU8) nanocomposites onto a gold layer or stripe (plasmonic waveguides), in order to provide gain to the propagating SPP when the nanocomposite is optically pumped.

- The second approach is also based on the use of infrared emitting QDs, but now using patterned SiN waveguides and electrical injection through applying an AC-field. We propose a hybrid platform where standard SiN waveguides are covered with an active QD layer (e.g. for modulation or light generation) and a cathode layer (for electrical contacting). We will use an ITO bottom contact in combination with a gold top contact to build the plasmonic waveguide.

In this report we summarize the results obtained in the plasmonic amplifier in both configurations including the design, a summary of the active materials and the experimental results. For this purpose this manuscript is based on the deliverables 4.1 [12] and 4.2 [13] were the design of the amplifiers and the description of the colloidal nanoparticles were thoroughly detailed.

# 2 Summary of colloidal QDs.

Deliverable 4.2 [13] described the different active materials studied in this project not only for the amplifier but also for the photodetector. In this report a summary is included in order to select the nanocrystals useful for gain applications and to update the information with nanoparticles synthetized recently. In this way the nanoparticles used in the amplifier device were CdSe QDs with emission at 600 nm, PbS QDs and PbS-based quantum rods with emission at 1550 nm and HgTe QDs with emission at 1550 nm.

## a. CdSe with emission at 600 nm

As explained in the introduction and deliverable 4.2 [13], QDs emitting at visible wavelengths have been used for preliminary investigations, given the vast literature background on these materials. Moreover, the chemistry to prepare nanocomposites layers has been found to be independent of the QD material and hence the implementation of infrared emitting nanoscomposites for waveguiding/amplification purposes is straightforward, despite the smaller signal-to-noise ratio in photodetection at NIR wavelengths. In particular, CdSe QDs was selected as an (available in-house in enough quantity) emitter to be incorporated in the plasmonic waveguides as preliminary tests. In this way, CdSe QDs were dispersed in appropriate concentrations on PMMA, and these colloidal solutions will be transformed in nanocomposite thin films once deposited on Si-$SiO_2$ substrates. Figure 2 shows the absorption and photoluminiscence (PL) spectra of the CdSe QDs used in this work. The PL peak was observed at 620 nm and the PL linewidth is around 40 nm. The main limitation of this sort of nanocrystals for gain applications is the reduced Stokes shift between the exciton absorption and emission peak wavelengths (about 40 nm), which leads to losses by reabsorption.

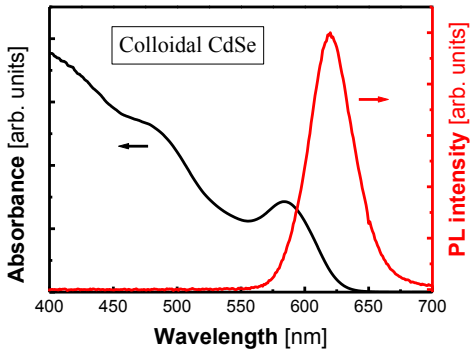


**Figure 2. Absorbance (black line) and PL (red line) spectra of CdSe QDs fabricated in UVEG.**

## b. PbS with emission at 1100-1550 nm

Since the target of Navolchi is to work in the 1400-1600 nm range it becomes necessary to use nanoparticles with emission at these wavelengths. For this purpose PbS based

QDs were initially chosen as active materials. Ground exciton peak transition of this sort of QDs can be tuned in the range 1300-1900 nm by using the procedure stablished by UVEG or UGent [13]. In this way PbS QDs synthesized by UGent have been initially supplied to UVEG. Figure 3a plots its absorption and emission spectra. Absorption curve (black line) shows the ground exciton transition at 1550 nm, but also the PL (red line), hence strong losses by reabsorption are again expected. Other PbS nanostructures with larger Stokes shift were synthetized by UGent and send to UVEG for further characterization in the form of dielectric waveguides based on QD-polymer nanocomposites. These nanocrystals were semiconductor quantum rods (QRs) with an elongated shape where the PbS core is covered by a CdS or CdSe shells. In this way surface traps are reduced by the shell passivation and the Stokes shift is enhanced because the absorption is determined by the shell volume (black line in figure 3b), while the emission is still occurring at the PbS core. In this way, PbS/CdS QRs (figure 3b), PbS/CdS partially exchanged rods (figure 3c) and PbS/CdSe QRs (figure 3d) with PL spectra (red linen) centered at 1350 nm, 1100 nm and 1400, respectively.

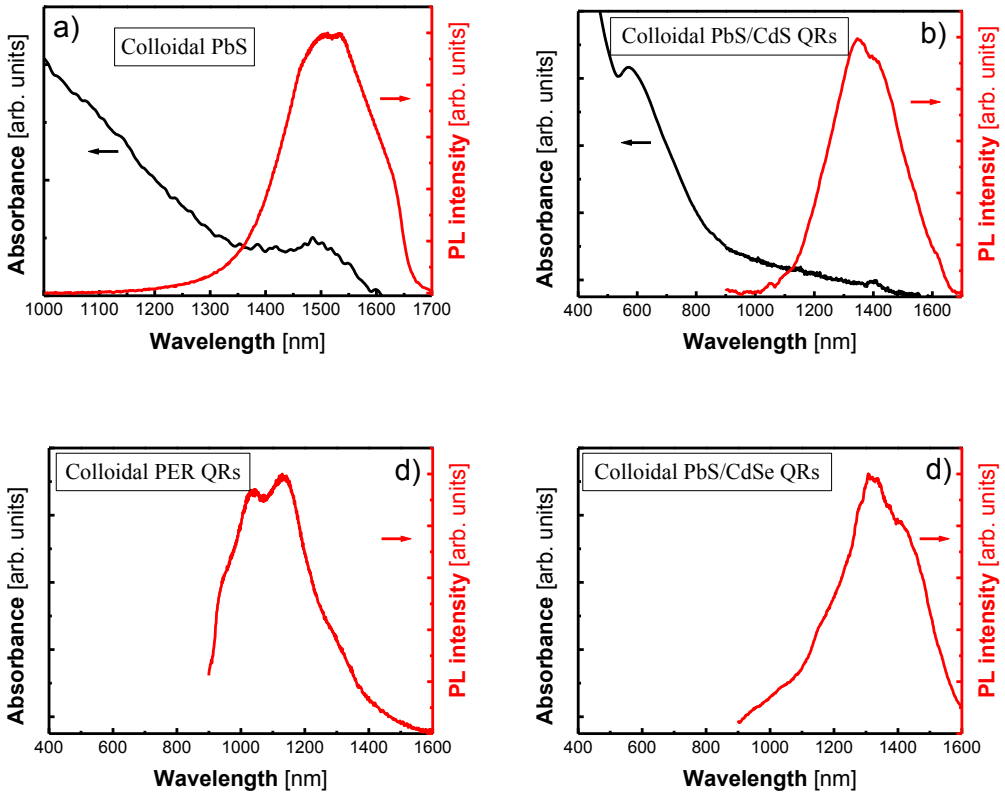


**Figure 3. Absorbance (black line) and PL (red line) spectra of PbS based QDs fabricated in UGent. a) spherical PbS QDs. b) PbS/CdS nanorods c) PbS/CdS partially exchanged nanorods d) PbS/CdSe QRs.**

## *c. HgTe with emission at 1550 nm.*

HgTe QDs were synthetized by UGent and sent to UVEG in order to complete a study of the most suitable material for amplification at infrared wavelengths. These nanocrystals seemed to be optimum for the target of the project since they have a broad emission range (1000-1400 nm), with a large Stokes-shift (100 meV) and long lifetime (≈40 ns). Figure 4 shows the

absorption and PL spectra in black and red lines respectively. The absorption curve shows the ground exciton peak placed at 1100 nm. Then it increases continuously for shorter wavelengths and decreases for longer ones. The absorption is negligible for wavelengths longer than 1300 nm. The PL peak has a Gaussian shape centered at 1350 nm with a FWHM of 200 nm. Finally, it is interesting to say that under the same pumping conditions and operation wavelength (1500 nm), these QDs showed the highest emission efficiency, so HgTe QDs are the material chosen to develop the plasmonic amplifier. Recently UGent improved the synthesis method resulting in much more clearly defined exciton peaks in the absorption spectra (Fig. 4b). Fig. 4b also shows these QDs can be synthesized with peak absorption wavelengths from 1200nm to 1550nm. Fig. 4c shows results from gain measurements carried out using a transient absorption setup (TA) on HgTe QDs in solution. An intrinsic gain up to 500 $cm^{-1}$ is measured over a wide spectral range. Extrapolating this intrinsic gain to a closed packed film this should allow for a gain of up to 100 $cm^{-1}$ . To confirm that these results are also relevant towards development of integrated optical devices, we alsoinvestigated the gain properties of HgTe QDs deposited in a thin film (spin coated 3 times on quartz). A slight red shifted is noted (50 meV). These samples were then analysed using transient absorption spectroscopy. Analysis of the results learns us (Fig. 4d):

- There is still gain present, shifted to the red side
- The gain occurs at similar fluences as before
- The gain lifetime is reduced however to ~ 100 ps.

We believe that the gain lifetime could be increased again through optimising the deposition process and possibly the synthesis. The main issue relates to avoiding photocharging in film. This work is in progress. Measurements on thicker films prepared in vacuum conditions should be investigated, as should the newly synthesized HgTe QDOTs with narrower size dispersions.

.

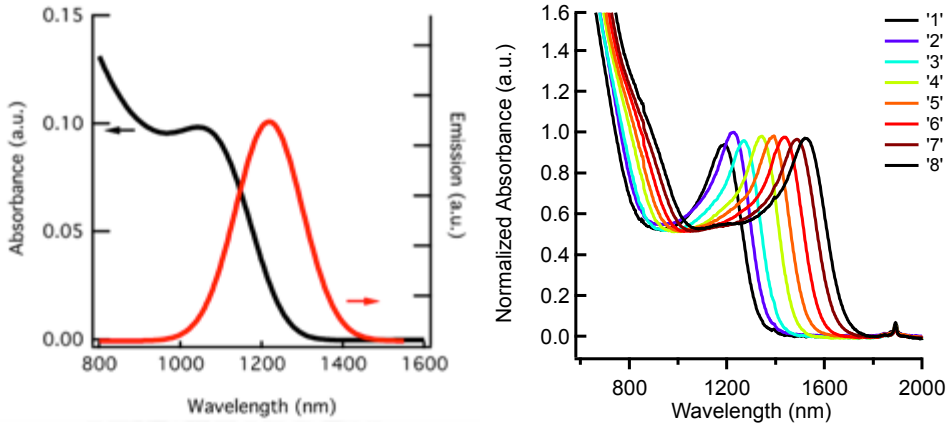

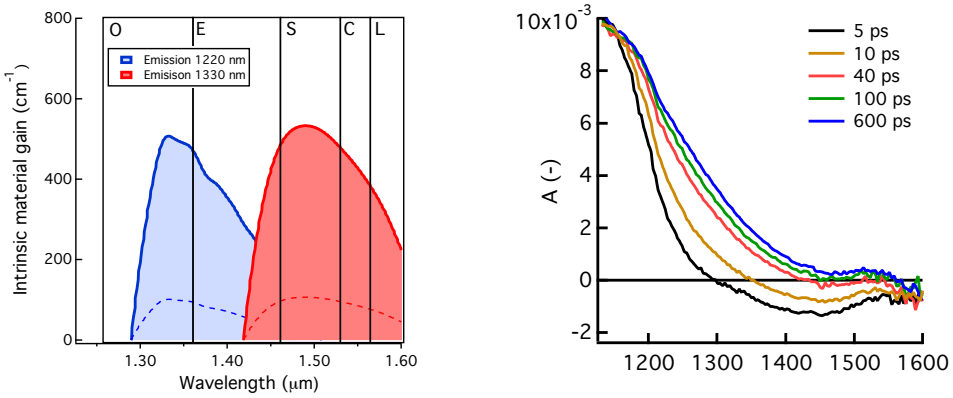


**Figure 4. a) Absorbance (black line) and PL (red line) spectra of HgTe QDs. b) Absorbance spectra of HgTe QDOTs with improved synthesis method.**

.

# 3 Plasmonic amplifiers based on nanocomposites.

The waveguides studied in this work are based on the structures shown in Figure 5. The basic structure (Fig. 5a) consists of a Au layer in contact with a nanocomposite with the intention to use the gain provided by the QDs to compensate losses of the propagating light along the Au-dielectric interface (SPP). Then, the bilayer Nanocomposite/Au is considered to be deposited on a $SiO_2$/Si substrate to integrate the plasmonic waveguide amplifier in a CMOS compatible substrate. Using this structure as a starting point the ones shown in Figures 5b, 5c, 5d and 5e were also considered. The plasmonic waveguide shown in figure 5b considers PMMA (or a QD-nanocomposite layer) between the $SiO_2$ and the Au in order to provide index matching. Also, it is interesting to integrate plasmonic waveguides together with dielectric ones in order to improve the propagation of the beams as it will be shown later. In this way, the waveguide depicted in figure 5c includes a top PMMA cladding to help the propagation of the light; and the structure shown in Figure 5d considers a patterning of the Au (in the shape of a stripe) in order to provide another degree of confinement and to profit the dielectric waveguide formed on the left and the right of the metal. Finally, waveguide shown in figure 5e considers a cladding PMMA layer in a symmetric structure. In all cases the thickness of $SiO_2$ is considered to be 2 μm that is thick enough to isolate the PMMA/Au and PMMA/Au/PMMA layers from silicon at the wavelength of interest.

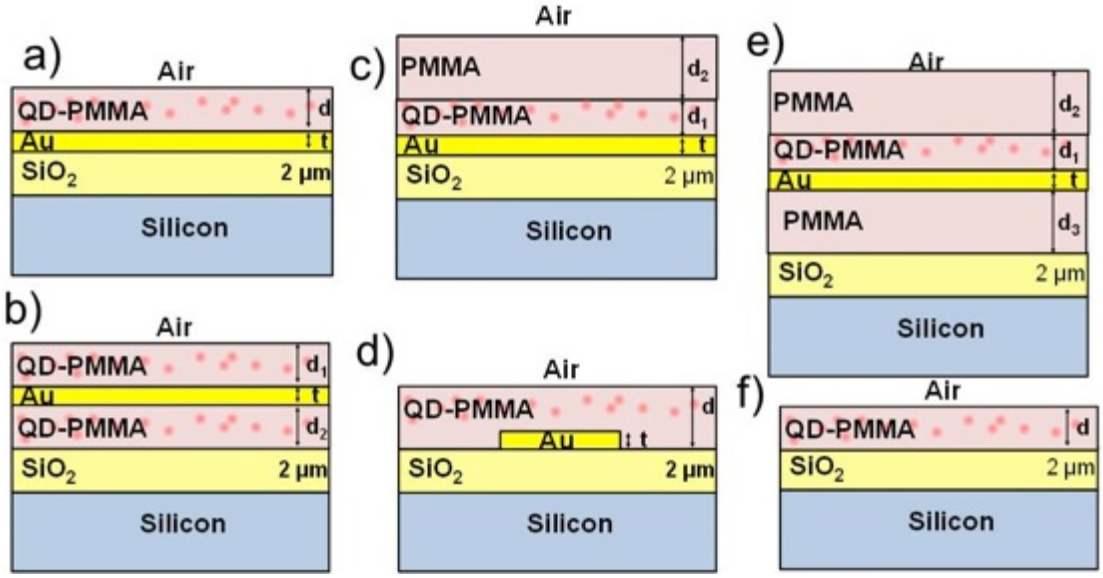


**Figure 5. Vertical cross sections of the plasmonic waveguides considered in the project.**

## *d. Design of plasmonic amplifiers.*

The design of the plasmonic amplifiers based on nanocomposites was thoroughly described in the previous deliverable [12]. Here a summary is included with the most important conclusions. The analysis consisted of by solving the propagation constant ($\beta$) or effective refractive index ($N_{eff}$) of the different modes allowed by the structure. Due to the fact that the metal is a lossy material, its refractive index is a complex number and with it the effective refractive index of the modes:

$$N_{eff} = N'_{eff} + iN''_{eff} \quad (1)$$

The real part (*Neff'*) is related with the group velocity of the light, and the imaginary part (*Neff''*) with the attenuation. Since the damping limits the propagation of the light in plasmonic waveguides, it is useful to define and the propagation length (*Lp*) as the distance where the intensity of light decays by a factor 1/e:

$$L_p = \frac{1}{2 \cdot k_0 \cdot N''_{eff}} \quad (2)$$

Here $k_0$ is the wave vector in vacuum ($k_0=2\cdot\pi/\lambda$) and $\lambda$ the operation wavelength. Then, $N_{eff}$ of the propagating modes in the structures were obtained by applying the transfer matrix method in the complex plane [14]. Table I summarizes the refractive indexes chosen for the materials at the working wavelengths. The coordinate system was chosen fixing the z axis along the propagation direction, whereas transverse x and y axe are perpendicular and parallel to the Au plane respectively. The insulator-metal-insulator (IMI) waveguide considered in this work has two solutions of bound plasmonic modes: the Long Range surface Plasmon Polariton (LR-SPP) with a symmetric shape of the transverse electric field ($E_x$), and the Short Range surface Plasmon Polariton (SR-SPP) with an asymmetric shape of $E_x$ [15]. In a practical point of view the first one is the most interesting since it reduces the attenuation for 2 or 3 orders of magnitude respect the second one [15], and it is the one considered in this work. A symmetric waveguide (Figure 5b) is able to propagate both the SR-SPP and LR-SPP with a different dependence on the Au thickness. However, in the asymmetric structure (figure 5a) there is a

cut-off on the LR-SPP mode below a certain thickness *t* that depends on the materials (refractive indexes) and operating wavelength.

| Material | 600 nm | 1550 nm |
|---|---|---|
| **Air** | 1 | 1 |
| **$SiO_2$** | 1.4582 | 1.4522 |
| **PMMA** | 1.489 | 1.483 |
| **Au** | 0.2203-3i | 0.439-9.519i |

**Table I. Material's refractive indices**

**Plasmonic amplifiers at 600 nm**

In [12] the behavior of asymmetric (Figure 5a) and symmetric (Figure 5b) waveguides were compared and it has been concluded that both structures provide the similar propagation length, but a better confinement can be achieved with the asymmetric one. Then, this design was selected for visible wavelengths. To optimize the thickness of the metal (*t*) a semiinfinite (PMMA/Au/$SiO_2$) was initially considered. Figure 6a shows the propagation length and mode confinements calculated with the method explained in [44] in a PMMA/Au/$SiO_2$ (open symbols) and PMMA/Au/PMMA (closed symbols) plotted as a function of the gold thickness at λ=600 nm (PL peak of CdSe, see Figure 1a). Metal thickness implies a trade-off between mode confinement and propagation losses [2]: the thicker the Au layer is the better the confinement of LR-SPP in the metal. However, thicker layers also imply a reduction in the propagation length due to the attenuation in the metal. Then a compromise has to be taken and the Au thickness was set to ***t= 30 nm***. The inset of figure 6b plots the intensity distribution of the LR-SPP for this thickness. The length of evanescent tail of the mode at $1/e^2$ in the nanocomposite is around 300 nm. When finite structures are taking into account not only the plasmonic modes, but also TE photonic modes and high order TM hybrid plasmonic-photonic modes can be propagated along the waveguide. Left axis of figure 6b shows the real part of the effective refractive index of the propagating modes as a function of the top cladding thickness (*d*) in the waveguide depicted in Figure 5a. High order TM modes are allowed when the cladding is thicker than $d>1.2\ \mu m$, and the cut-off for TE polarization is around to $d=0.7\mu m$. Also, it is important to contemplate that the cladding should be thick enough to keep the evanescent tail of the LR-SPP which it extends about 300 nm at $1/e^2$ (see inset of Figure 6a). In this way right axis of the Figure 6b (continuous red line) refers to the Lp of the LR-SPP mode as a function of the nanocomposite thickness *d*. It increases for thin cladding films, and then it saturates to the length obtained for semi-infinite condition (see Figure 6a). Thus, the thickness of the nanocomposite has been fixed to be around ***d=1 μm*** in order to avoid high order propagating modes in TM and additional losses. The inset of Figure 6b shows the intensity distribution of the LR-SPP and the $TE_0$ modes at λ=600 nm using *t=30* nm and $d=1\ \mu m$. Plasmonic LR-SPP has a Lorentzian distribution with a FWHM of 170 nm and it is centered in the gold whilst the photonic TE mode has a quasi-Gaussian shape confined in the PMMA with a FWHM of $0.6\ \mu m$. Propagation length of the modes are $Lp=1.2\ \mu m$ in the LR-SPP and $Lp=200\ \mu m$ considering a filling factor of QDs in the PMMA of *ff=1%* and $\lambda=600\ nm$

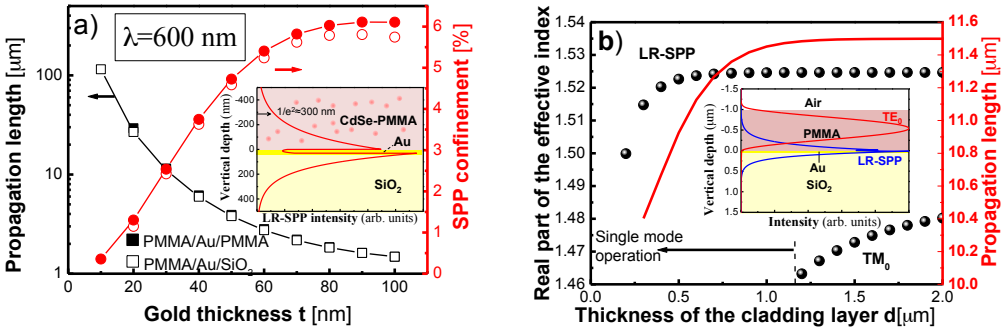


**Figure 6. a) Propagation length (blue line and left axis) and mode confinement (red line and right axis) of the LR-SPP mode propagating in a CdSe-PMMA/Au/$SiO_2$ structure as a function of the Au thickness (t). The inset plots the intensity distribution of the LR-SPP for *t=30 nm*.**

The plasmonic waveguide shown in figure 5a has been optimized to obtain the better compromise between mode confinement and propagation losses, and to avoid the presence of high order TM modes. However, to amplify the signal carried by the metal it becomes necessary to excite the structure by means of a pump beam with a wavelength below the band-gap of the nanoparticles. For this purpose a common method to pump the waveguide is focusing the pump beam on the top of the sample in the shape of a straight line by using the variable stripe length method [7, 12, 16-17]. However, although this experimental set-up allows a uniform excitation along the entire length of the waveguide it has the drawback of a reduced pump power density (line area is around $10^5$ μm$^2$). To solve this problem an efficient solution is to couple and propagate the pump beam along the waveguide. In this way, light is confined in the reduced dimensions of the core of the structure (1-10 μm$^2$) and pump power density increases. However, propagation of light in plasmonics waveguides is limited by the absorption of the Au, and at $\lambda$*=600 nm* propagation length of the photonic $TE_0$ mode has been limited to 200 μm. Moreover, losses increase at short wavelengths (necessary to pump the nanocrystals) because not only of a stronger attenuation of the metal, but also a higher absorption of the nanocrystals (see figures 3-4). Nevertheless, this limitation can be resolved when a thick enough PMMA cladding is deposited on the nanocomposite [18], because most of the pump beam can be coupled into the cladding where the absorption is smaller than the one present in the nanocomposite or the metal. The design of the structure is drawn on figure 2c and consists of a nanocomposite (with thickness $d_1$) deposited in the metal (thickness $t$) and on the top of the waveguide a layer of PMMA (of thickness $d_2$). The idea of the pump coupling/extraction of light is shown in figure 7. First, the pumping beam is coupled into the PMMA cladding. Since most part of the mode is confined in this layer (where there is no absorption) it can propagate through the structure coupled to photonic modes in this layer (figure 7a). Nevertheless the tail of the mode overlaps with the nanocomposite, exciting in consequence the QDs when the pump beam travels through the waveguide (figure 7b). Then, the PL can be coupled to the different waveguide photonic or plasmonic modes. Indeed, a thick cladding layer would imply the presence of high order TM modes and the signal at the output of the structure will be composed of photonic and plasmonic modes and not only by the SPP. But, with an appropriate choice of the thickness of the layers, the overlap of the nanocomposite can be maximized to the SPP field distribution, and in consequence most of the PL will be coupled only to the SPP rather than photonic modes (figure 7c). In this way, in order to maximize the interaction of the SPP with the gain material it is useful to match the tail of the SPP with the nanocomposite. Then, $d_1$ was fixed equal to ***$d_1$=250 nm*** because it is

close to the evanescent tail in the PMMA. The thicknesses of the top cladding ($d_2$) needs to be thick enough to allow the propagation of the pumping beam with low propagation losses together with enough interaction with the nanocomposite layer to achieve an efficient excitation of the nanocrystals, and it has been to be around ***$d_1$=5.0 μm*** in the study carried out in [12].

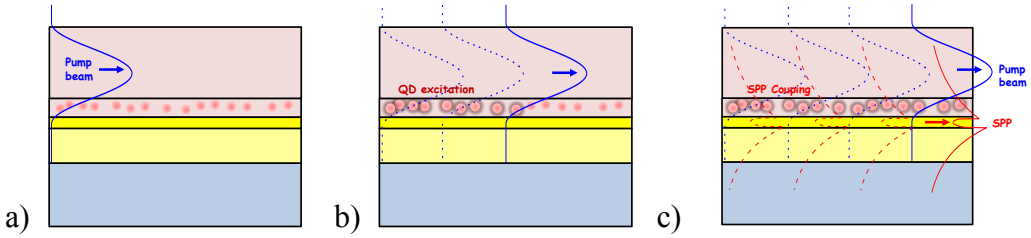


**Figure 7. Plasmonic coupling through a cladding layer.**

Moreover, propagation of the pump beam can be also enhanced by a combination of the plasmonic waveguides with dielectric ones, which usually show smaller propagation losses. In this way the design shown in figure 5d is also proposed to complement this study. This waveguide consists of a Au stripe patterned on the $SiO_2$/Si substrate and with a QD-PMMA layer deposited on the top of the structure. Then plasmonic modes will achieve another degree of confinement that depends on the width of the stripe. Figure 8a plots the effective refractive index of the fundamental LR-SPP mode (red line and left axis) and its respective propagation length (blue line and right axis) as a function of the Au width calculated with the effective index method [14]. Thicknesses of the gold ($t$) and the dielectric ($d$) were fixed to 30 nm and 1 mm respectively, and the operation wavelength was $\lambda$=*600 nm*. The curves have three different regions. If the width is ranged between 0.1 and 1 μm, the narrower the longer the propagation length propagation length and the lower its effective refractive index metal. This is because the mode is more and more spread in the dielectric as it is shown in figure 8b where the fundamental LR-SPP is plotted for different stripe widths. But, if the width is below or above this value both parameters reaches saturation. Also, it is important to say that for stripes wider than 1 μm the LR-SPP is spread into horizontal modes with similar propagation length. Indeed, if the width of the stripe is wider than 4 μm there are more than 7 horizontal modes allowed in the waveguide, and it can be considered as a planar structure similar to the one depicted in figure 5a. Nevertheless, the pattern of the metal allows the presence of a dielectric waveguide on the left and the right of the Au. Then, if the filling factor of QDs in the PMMA is chosen properly [10] this waveguide can help the propagation of a pump beam in a similar way that it did in the bilayer structure shown in figure 5b.

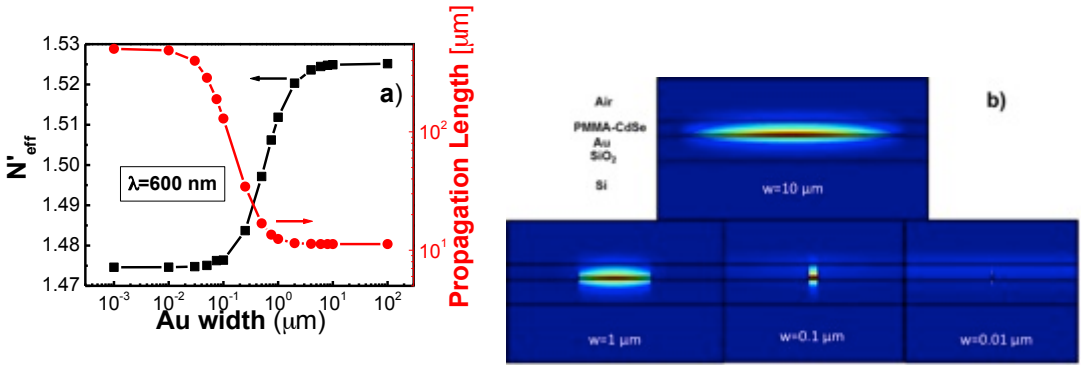

**Figure 8. a) Effective refractive index of the fundamental LR-SPP mode (red line and left axis) and its respective propagation length (blue line and right axis) as a function of the Au width. b) Fundamental LR-SPP mode distribution for different stripe widths (w).**

## Plasmonic amplifiers at 1550 nm

Symmetric and asymmetric waveguides (with the structure shown in Figures 5a and 5b respectively) were carefully analyzed at an operation wavelength of 1550 nm in [12]. Firstly it has been concluded that when semi-infinite (PMMA/Au/$SiO_2$) waveguides were considered the LR-SPP is under cut-off in the asymmetric waveguide for Au layers thinner than *60 nm*. The symmetric (PMMA/Au/PMMA) structure however, can guide this mode for all thicknesses. Figure 9a plots the propagation length (left axis and blue line) and the mode confinement (right axis and red line) of the LR-SPP as a function of the Au thickness in the symmetric (filled symbols) and asymmetric (open symbols) semi-infinite waveguides. Again, an optimum thickness was found for ***t=30 nm***. By chosen this parameter propagation length reaches the mm range while the mode confinement is reduced to 0.05 %. This is due to the long evanescent tail of the mode (around 2 μm at 1/e) as it is shown in Figure 9b, where the mode distribution of the LR-SPP is depicted in red line. Finally, it is important to say that both waveguides support the SR-SPP mode. By choosing the thickness of *t=30 nm* this mode is strongly confined in the metal with a confinement factor of around *0.4 %*, and propagation lengths of *11.4* and *12.8 μm* in the symmetric and asymmetric structures respectively. Then, although at visible wavelengths this mode was not considered because the propagation length was shorter than *1 μm*, it could be necessary to take in account at long wavelengths. Green line of Figure 9b draws field mode distribution of this mode in the symmetric waveguide (in the asymmetric one the SR-SPP shows a similar profile).

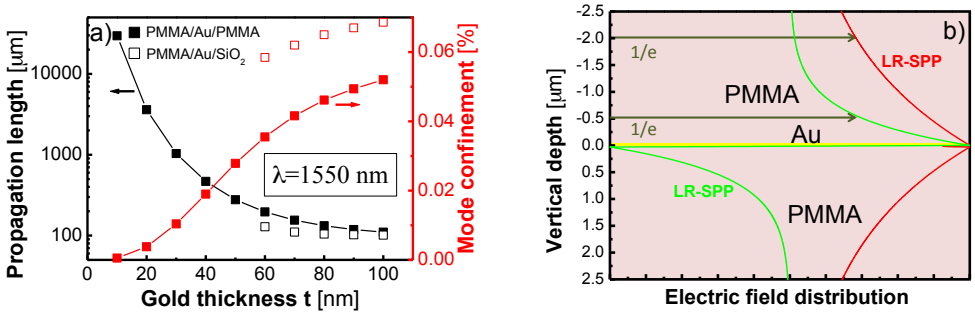


**Figure 9. a) Propagation length and confinement factor as functions of the gold thickness (*t*) at *λ= 1550 nm* b) Mode distribution of the LR-SPP and SR-SPP at *λ= 1500 nm* using *t=30 nm* and the symmetric waveguide.**

When finite claddings are considered not only plasmonic modes, but also hybrid photonic-plasmonic modes are allowed in both the asymmetric and symmetric waveguides [12]. Figure 10a plots the effective refractive index (left axis) and the propagation length of the fundamental $TM_0$ mode as a function of the cladding layer (*d*) in the asymmetric structure (Figure 5a). The waveguide presents single mode operation for claddings thinner than 4 μm, but due to the fact that the structure cannot propagate the LR-SPP the fundamental mode exhibits hybrid photonic-plasmonic nature extended in the PMMA and the $SiO_2$ [12]. Then, because of the small interaction of the metal this mode shows a long propagation length. The

inset in the figure plots the power mode distribution of the $TM_0$ and $TE_0$ modes when $d=3\ \mu m$. Fundamental $TM_0$ mode is distributed between the PMMA and the $SiO_2$, whilst the $TE_0$ is confined in the polymer. Left axis of figure 10b plots the effective refractive indexes of the TM modes in the symmetric waveguide (Figure 5b) as a function of the top cladding thickness ($d_1$). The bottom cladding thickness ($d_2$) was set to $d_2=2\ \mu m$. This structure is able to guide the LR-SPP and avoids the propagation of TM photonic modes for cladding thinner than 4 µm. The *Lp* of the LR-SPP, shown on the right axis of the Figure 10b, increases with cladding thickness and reaches saturation to around 0.9 µm for $d_1=4\ \mu m$. Then, at infrared wavelengths the Lp of the LR-SPP is increased by 10-fold respect that found at visible operation (see Figure 6b). This due to the longer evanescent tails of the modes, as it is shown in figure 9b or the the inset of Figure 10b, where the power distribution of the LR-SPP (continuous line) and $TE_0$ (dash line) is plotted for $d_1=3\ \mu m$ and $d_1=2\ \mu m$. Again, plasmonic mode is centered on the metal and photonic mode on the polymer. Finally, it is interesting to say that both structures can support the SR-SPP with a similar distribution as that shown in Figure 9b.

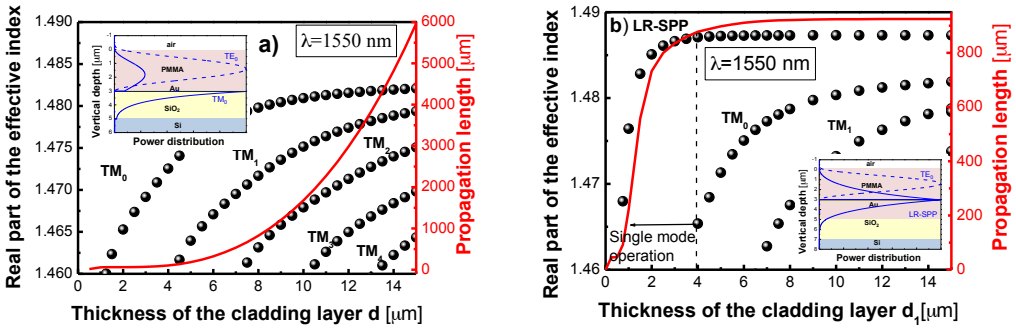


**Figure 10. Real part of the effective refractive index and propagation length as a function of the thickness of the cladding layer ($d_1$). a) Asymmetric waveguide. b) Symmetric waveguide choosing $d_3$=3 µm. The inset shows the power distribution of the fundamental modes.**

## e. Fabrication of the waveguides.

The waveguides depicted in Figure 5 were fabricated by using the following procedure. In asymmetric waveguides (Figure 5a and 5c) Au layer is evaporated on a commercial $SiO_2$/Si substrate supplied by Cemat Silicon S.A. Then CdSe-PMMA nanocomposite is spin coated on the metal by using the procedure explained in [10]. In the case where a bilayer waveguide is considered (figure 5c) the top PMMA cladding is deposited on the nanocomposite by the same method. Symmetric waveguides (Figures 5b and 5e) were fabricated following the same steps, with an initial deposition of PMMA previously to the Au evaporation. In sample shown in Figure 5e Au stripes are made by a standard lift-off process. Finally, sample shown in Figure 5f consists of a dielectric waveguide fabricated by spin coating the nanocomposite on the $SiO_2$/Si substrate and is used to compare the gain material in a system with lower propagation losses.

## f. Characterization of dielectric waveguides.

Figure 11 shows the experimental set-ups used to characterize the samples. The set-up shown in figure 11a consists of the standard end fire coupling system where an input beam is coupled from one edge of the sample with the aid a microscope objective, and the light at the output is collected with another microscope objective that can focus it to a CCD camera or a spectrograph. If the wavelength of the pump beam is short enough to pump efficiently the QDs, they will emit their PL which is then waveguided through the structure together with the pumping beam. Then, at the output of the system, a high pass filter is included in order to separate the PL from the pump beam. However, the designs shown in figure 2b are difficult to be characterized with this set-up, because strong attenuation in the gold limits the propagation length of the modes to 10-100 μm, and samples with such a length are difficult to fabricate and manipulate. The set-up shown in figure 5b avoids this problem. It consists of focusing the pump beam on the surface of the sample in the shape of the straight line with the aid of a cylindrical lens. In order to avoid the influence of the Gaussian profile of the laser, a slit was used and to keep the central 1.4 mm of the beam, where it is approximately constant. In these conditions, the pump power is constant in the whole length of the pump line and hence the QDs are excited homogeneously on the structure. Then the propagation of signal PL in waveguide follows the equation:

$$\frac{dI_v(x)}{dx} = I_{SS} + (g - \alpha) \cdot I_v(x), \quad (3)$$

where $I_v$ is the intensity of the light, $I_{SS}$ the intensity of the spontaneous emission, g the gain and α the losses. Then, gain of the structure can be estimated by measuring the emission as a function of the strip length ($d$) by the variable stripe length (VSL) method [9]. Also, as long as the sample is more concentrated, the slope in the gain is fast. When saturation is absent, the gain of the structure can be calculated as:

$$I(d) = \frac{I_{SS}}{g-\alpha} \cdot \left(e^{(g-\alpha)\cdot d} - 1\right). \quad (4)$$

However, in the presence of saturation, the gain obeys the following law [17]:

$$g = g_0 \cdot e^{-d/L}, \quad (5)$$

where $g_0$ and $L$ are fitting parameters related with the gain and the saturation. Similarly, the attenuation of the waveguide can be characterized by keeping the length of the stripe constant and moving it away from the edge of the sample. Then, propagation losses can be fitted by approximating the dependence of the output intensity as a function of the distance between the stripe and the edge of the sample ($x$) with an exponential decrease:

$$I(x) \propto e^{-\alpha \cdot x} \quad (6)$$

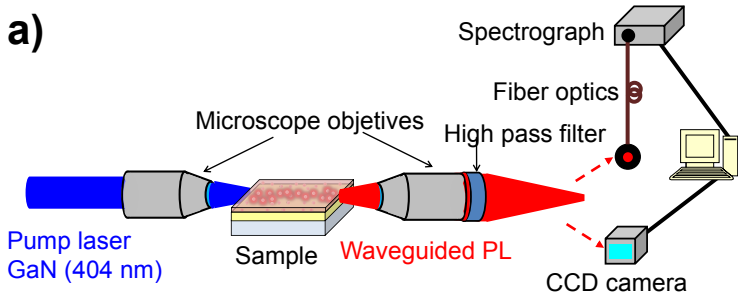

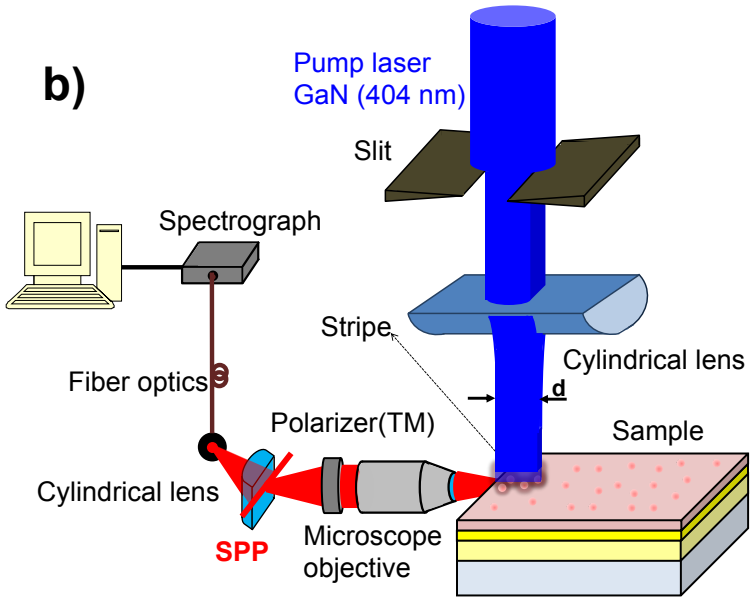


**Figure 11. a) Experimental set to couple light from the edge of the sample. b) Experimental set-up to pump from the surface**

The following sections will summarize the gain and losses characterization with the different quantum dots materials described in section 2.

### c.1. CdSe-PMMA

Figure 12 shows VSL characterization on CdSe-PMMA waveguides with different concentrations of CdSe in PMMA ($ff=2.6\cdot10^{-4},1.7\cdot10^{-3},4.4\cdot10^{-3},8.8\cdot10^{-3}$). Figure 12a plots the PL intensity as a function of the stripe excitation length; symbols correspond to the experimental data and red straight lines to the modelling using equations (4-6). The signal increases significantly with the length of the stripe and reaches saturation for lengths between 300 and 900 µm, depending on the concentration. The model fits well the experimental data by setting $L$ between 200 and 250 µm (these values are similar for all materials and will be fixed in all fits) and values of $g_0$ for different $ff$ are given in the plot. The value of $g_0$ obtained from the best fits tends to increase with $ff$ due to the growing amount of QDs absorbers/emitters. However, the propagation losses also increase in the same proportion due to reabsorption effects [17]. Figure 12b shows the dependence of the PL intensity as a function of the distance between the stripe and the edge of the sample (keeping the strip length constant) in the four samples studied in figure 12a; the losses increases from 26 to 61 $cm^{-1}$ from the lowest to the highest $ff$. In all cases losses are similar or bigger than $g_0$ and hence net gain is not reached. A first strategy to solve this issue is the use of other semiconductor nanostructures with larger Stokes shift than spherical QDs in order to reduce reabsorption effects along the propagation of the PL signal beam, as corroborated below by using semiconductor nanorods.

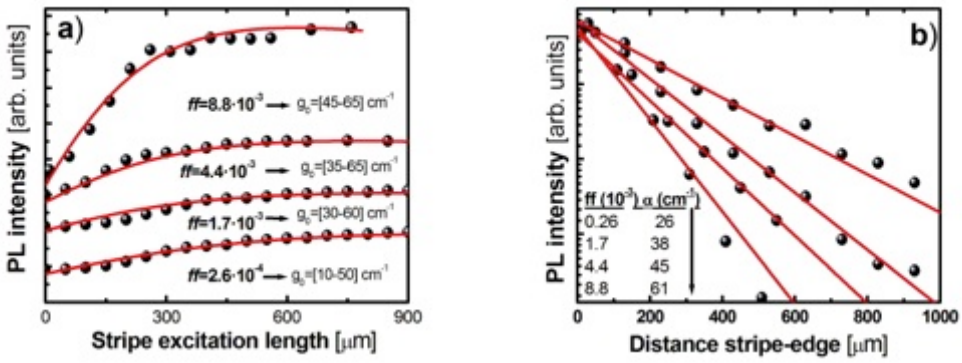


**Figure 12. VSL method in CdSe-PMMA dielectric waveguides. a) PL intensity as a function of the stripe excitation length b) PL intensity as a function of the distance between the stripe and the edge of the sample. The detection wavelength is that of the PL peak (600 nm).**

## c.2. PbS-PMMA

Figure 13 shows the application of the VSL to waveguides made by dispersing PbS QDs in PMMA using an intermediate concentration of *ff* =0.04. The best fitting values of $g_0$ are ranged between 60 and 80 $cm^{-1}$ (Figure 13a), but again the losses (Figure 12b) are more important (90 $cm^{-1}$) preventing amplification.

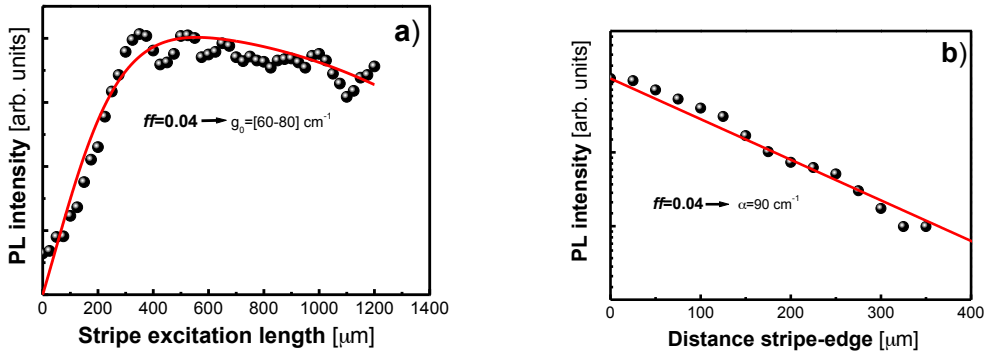


**Figure 13. VSL method in PbS-PMMA dielectric waveguides. a) PL intensity as a function of the stripe excitation length b) PL intensity as a function of the distance between the stripe and the edge of the sample. The detection wavelength is that of the PL peak (1550 nm).**

## c.3. PbS/CdS PMMA

Figure 14 shows the VSL characterization in a waveguide made by the dispersion of PbS/CdS semiconductor nanorods in PMMA with *ff=0.04*. In this case $g_0$ reaches a value around 120 $cm^{-1}$, slightly larger than that found above for spherical core-QDs (in PMMA nanocomposites with the same *ff*), whereas losses are reduced to 70 $cm^{-1}$. Therefore, one could say that net gain could be possible in waveguides fabricated with this kind of nanostructures if their length is shorter than 400 mm, before the observed intensity saturation in Figure 14a. This means that our previous hypothesis of reducing reabsorption losses by using semiconductor nanoparticles with larger Stokes-shift was correct.

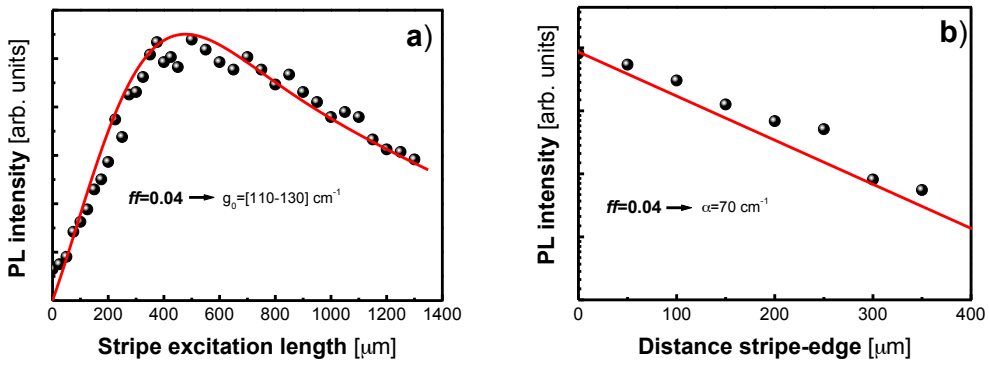


**Figure 14. VSL method in PbS/CdS-PMMA dielectric waveguides. a) PL intensity as a function of the stripe excitation length b) PL intensity as a function of the distance between the stripe and the edge of the sample. The detection wavelength is that of the PL peak (1400 nm).**

## c.4. PER-PMMA

Figure 15 shows the VSL results obtained on PMMA waveguides containing PER nanorods; two different *ff* values were used 0.01 and 0.06. In the sample with the highest concentration $g_0$ can reach values up to 370 $cm^{-1}$ with losses limited to 100 $cm^{-1}$. Again, net gain and amplification would be possible with this kind of nanoparticles within a waveguide length shorter than 250 μm. In the sample with *ff=0.01* the gain is much lower and closer to the losses factor (16 $cm^{-1}$). We can also say that attained nanoparticle concentration in the PMMA-nanocomposite (6 times), whereas losses increase in a similar amount, as expected.

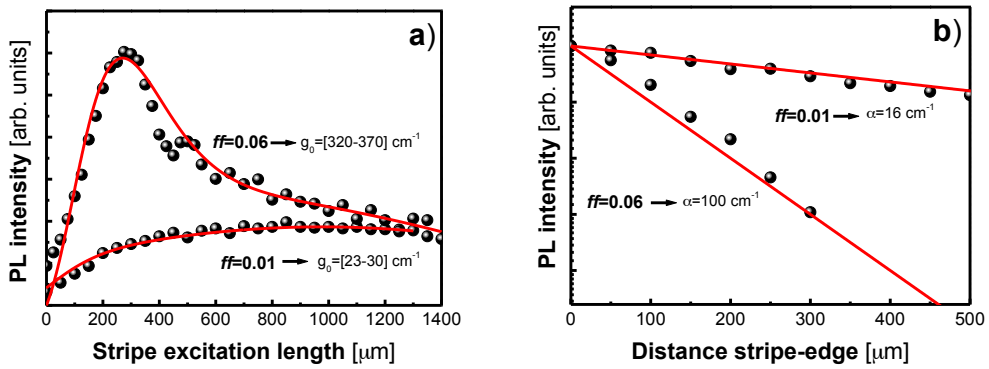


**Figure 15. VSL method in PER-PMMA dielectric waveguides. a) PL intensity as a function of the stripe excitation length b) PL intensity as a function of the distance between the stripe and the edge of the sample. The detection wavelength is that of the PL peak (1100 nm).**

## c.5. PbS/CdSe-PMMA

Figure 16 shows the VSL results obtained in a waveguide made by dispersing PbS/CdSe nanorods in PMMA with *ff=0.04*. The best fitting value for case $g_0$ is around 150 $cm^{-1}$, very similar to the case of PbS/CdS nanorods, but for a maximum waveguide length 200 μm. Again, the large Stokes shift in these nanostructures yields $g_0$ value higher than the losses factor (16 $cm^{-1}$). The main difference between both kind of nanorods, CdS versus CdSe shell materials, can lie in the band alignment between shell and core materials, introducing

different confinement conditions for electron and holes and hence influencing the excitonic transition and Auger recombination rates.

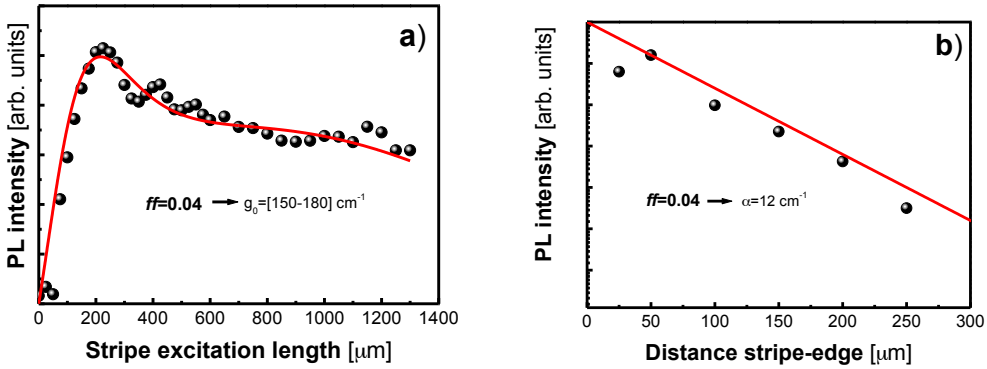


**Figure 16. VSL method in PbS/CdSe-PMMA dielectric waveguides. a) PL intensity as a function of the stripe excitation length b) PL intensity as a function of the distance between the stripe and the edge of the sample. The detection wavelength is that of the PL peak (1300 nm).**

## c.6. HgTe-PMMA

Figure 17 plots the VSL results measured in a waveguide made by dispersing HgTe QDs in PMMA with *ff=0.008* and *0.08*. In these samples $g_0$ reaches similar values (around 250 $cm^{-1}$) for both concentrations, while losses are significantly reduced to 30 $cm^{-1}$ in the sample with the lowest *ff*. Only PER-nanorods in a high *ff*-sample exhibited a higher value of $g_0$ (Figure 15), but in that case the sample showed also high losses (up to 100 $cm^{-1}$). Indeed, only samples with PbS/CdSe QRs and PER QDs (under small concentration) exhibited smaller propagation losses, but in those cases $g_0$ was reduced down to 160 and 40 $cm^{-1}$, respectively.

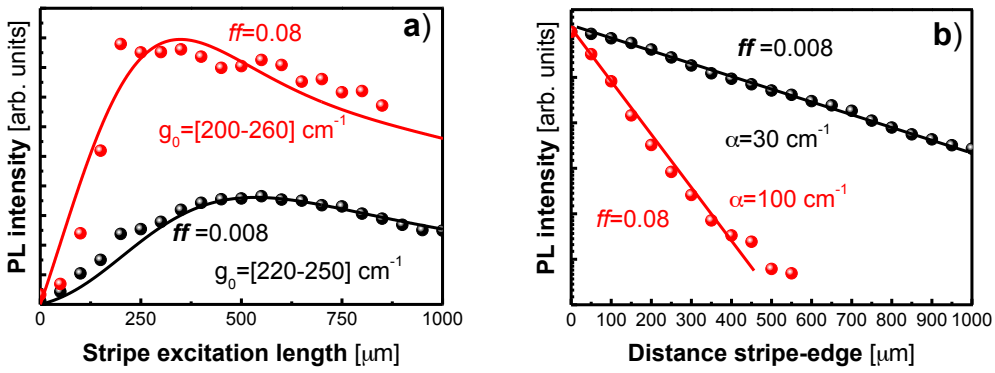


**Figure 17. VSL method in HgTe-PMMA dielectric waveguides. a) PL intensity as a function of the stripe excitation length b) PL intensity as a function of the distance between the stripe and the edge of the sample. The detection wavelength is that of the PL peak (1400 nm).**

Finally, it is interesting to note that PL band of HgTe-PMMA nanocomposites exhibit significant changes with pump power. Figure 18 plots the waveguided PL spectra under low (Fig. 18a) and high (Fig. 18b) pump power conditions in tbe sample with *ff=0.08*. Clearly, the

PL band broadens toward the high energy (short wavelength) side under high power excitation conditions. This behavior can be accounted for by using two Gaussian curves (green dashed lines) to convolute the whole PL band (red continuous line over open symbols), centered at *0.907 eV* (linewidth ≈ 84 meV) and ≈ *0.975 eV* (linewidth ≈ 150 meV). The low energy Gaussian dominates the PL spectrum under low pumping power conditions (Fig. 18a), whereas the high energy one becomes more important and eve dominates by increasing pump power (Fig. 18b). Figure 18c shows the integrated intensity of the Gaussian curve as a function of the pump power in a logarithmic scale; the low (high) energy PL-component exhibit a sub-linear (linear) dependence with the pump power, which could be attributed to a transfer dynamics between both excitonic populations. There is not a clear explanation on the origin of the high energy PL component without further experiments.

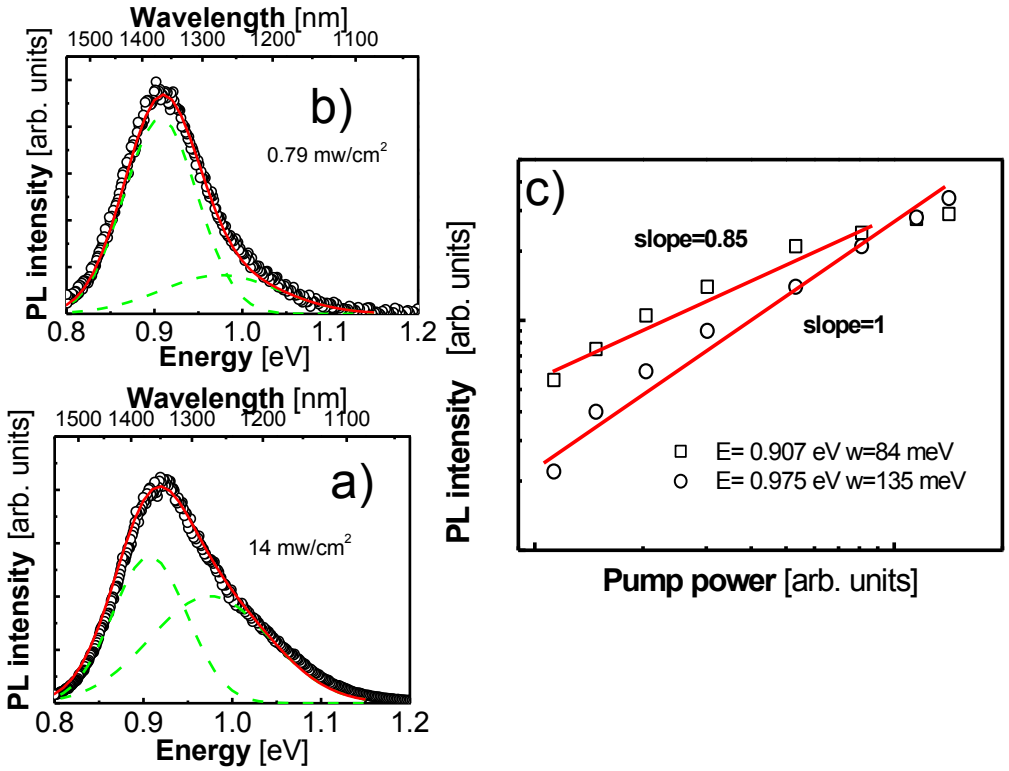


**Fig. 18. PL spectra of a HgTe-PMMA Sample (*ff*=0.08) pumped from the surface with a GaN laser (404 nm). a) PL spectra pumped with 0.79 mW/cm$^2$. b) PL spectra pumped with 14 mW/cm$^2$. Symbols, green dash lines and continuous red lines correspond to experimental points, Gaussians and curve fitting respectively. c) PL intensity as a function of pump power for the two Gaussian curves.**

## *d. Characterization of plasmonic waveguides.*

In previous reports we started the characterization of plasmonic waveguides by using the end fire coupling set-up or the VSL method, but it was not possible to measure accurately the propagation length of the plasmonic modes. The excitation of the SPP requires light

focusing on a small area (to optimize the coupling in a specific zone) and the shift of this pumping-focus along the waveguide to study the attenuation of the SPP and hence deduce the SPP propagation length ($L_p$). For this purpose, a new method was developed to characterize our plasmonic waveguides, based on the use of a monomode bare fiber ended with a sharp round tip (Figure 19a). When the fiber tip is approximated to the sample the pumping light of appropriate wavelength can be focused into a reduced spot of 2-3 $\mu m^2$ and the spontaneous emission of QDs in the gain material can be coupled to the propagating waveguide modes (Fig. 19b). In this way, the PL signal as a function of the distance between the tip and the edge of the sample (z) can be analyzed, as it is shown in Fig. 19c, in order to deduce the SPP propagation length.

Finally, we study the enhancement of Lp on the propagating LR-SPP along the Au waveguide by using an additional pump beam able to generate the gain in the nanocomposite and hence compensate the losses in the metal. This second excitation pump beam has to be powerful enough along the entire propagation of the LR-SPP in the waveguide, as compared to the low power of the laser light coupled to the fiber tip that generates the LR-SPP. The plasmonic/nanocomposite structure can be pumped from the top to achieve a uniform excitation [7], but the excitation area is very large and the pump power density very low to produce the desired gain. The more complex designs shown in Figs. 5c-d-e can overcome this problem by using dielectric waveguides to propagate the pump beam along a cladding layer with low propagation losses (Fig. 7), whose results are shown below.

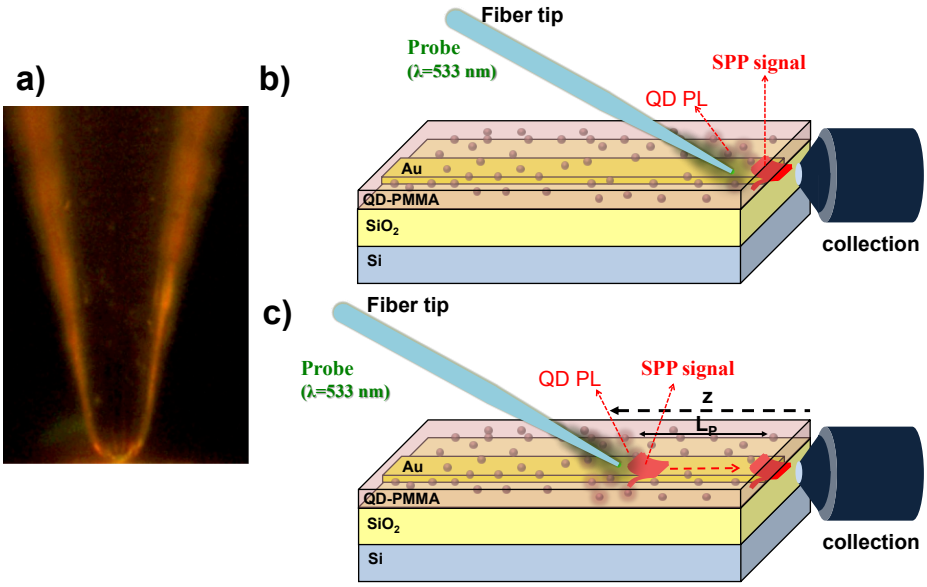


**Figure 19.** a) Fiber tip. b) SPP excitation with a fiber tip; if the excitation wavelength (532 nm in our case) is smaller than the QD band-gap the tip probe excites the QDs and their PL is coupled to the waveguide modes (LR-SPP mainly). c) Deduction of Lp from the intensity variation as a function of the distance between the tip probe and the edge of the sample.

### d.1. CdSe-PMMA with emission 600 nm

Fiber tip characterization set-up (Fig. 19) was firstly tested and validated with the plasmonic planar waveguides shown in Figure 5a by choosing CdSe QDs as active medium. It consists of a CdSe-PMMA nanocomposite deposited on a Au-film evaporated onto a $SiO_2$/Si substrate. The filling factor of QDs in the polymer was fixed to $ff=10^{-3}$ in order to obtain a good compromise between signal generated and reabsorption [10]; and the thickness of the

Au and the polymer were fixed to *t=30 nm* and *d=1 μm* as it was explained above. Figure 20a shows the near field images of spontaneous emission from QDs coupled to the guided modes under TM and TE polarizations using the fiber tip set-up in this waveguide (excitation laser: 533 nm, continuous wave). Clearly, TE and TM modes show a different light distribution because the first one is centered in the polymer and the second one in the metal (see inset of Figure 6b). When light was analyzed as a function of the distance between the tip and the edge of the sample a single exponential decay was obtained (Figure 20b). From the slope of this decay it is possible to extrapolate $L_p$ of the modes by fitting (continuous line) the experimental data (symbols) by means of the equation:

$$I_{PL} = A \cdot e^{-z/Lp} \quad (7)$$

where A is a fitting constant. TE polarization shows smaller propagation losses with a Lp in the range 50 - 71 μm (absorption and scattering losses in the nanocomposite), while TM polarization corresponds to the LR-SPP and its Lp results in the order of 10.5 - 14.3 μm, which are in very good correspondence with our simulations (11 μm).

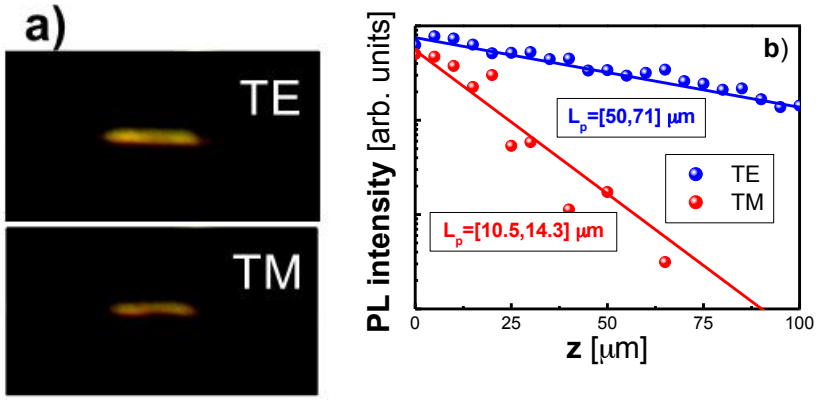


**Figure 20.** Characterization with the fiber tip method of a sample with the structure shown in Figure 5a at 0.6 μm: a) Near field images of TE and TM optical modes and b) PL intensity variation for TE (blue symbol) and TM (red symbols) as a function of the distance between the tip and the edge of the sample. Lp are extracted from a single exponential decay fitting (continuous lines).

Although this planar waveguide (Fig. 5a) can be used to demonstrate the coupling between colloidal QDs to plasmonic modes, we are not able to induce an enhancement of the SPP propagation length, because the structure cannot propagate a pump beam by end fire coupling and the vertical pumping is unefficient. For this reason a new metal/nanocomposite structure (Fig. 5c) was proposed to allow for an efficient pumping of QD emitters along the SPP propagation; it is based on a CdSe-PMMA/PMMA bilayer deposited on the Au layer in order to use the PMMA cladding, where the pump beam can propagate long distances, as illustrated in Fig. 7. Most of the emitted light is expected to couple to the LR-SPP, because this is the mode with the highest overlap with the nanocomposite (Fig. 7). Figure 21 shows the near field characterization (a) and the dependence of the $L_P$ intensity as a function of the distance between the tip and the edge of the waveguide (b) in a sample with *ff=0.1 %*, *t= 30 nm*, $d_1$*=250 nm* and $d_2$*=2 μm*. The spatial distribution of the optical mode is different for TE and TM polarizations for only the fiber tip probe excitation (laser at 533 nm) and both the fiber tip and pump beam excitation (laser at 405 nm). Moreover, the TM signal exhibits higher propagation losses (solid symbols in Fig. 21b) than those measured under TE (open symbols in Fig. 21b). The TM decays are fitted through eq. 7 (continuous lines) by Lp in the

range 8.3 - 12.5 μm, very close to the theoretical value (11 μm), whereas Lp increases up to 20 and 33 μm for pumping laser powers of 740 (red) and 2000 (green) W/cm$^2$ respectively.

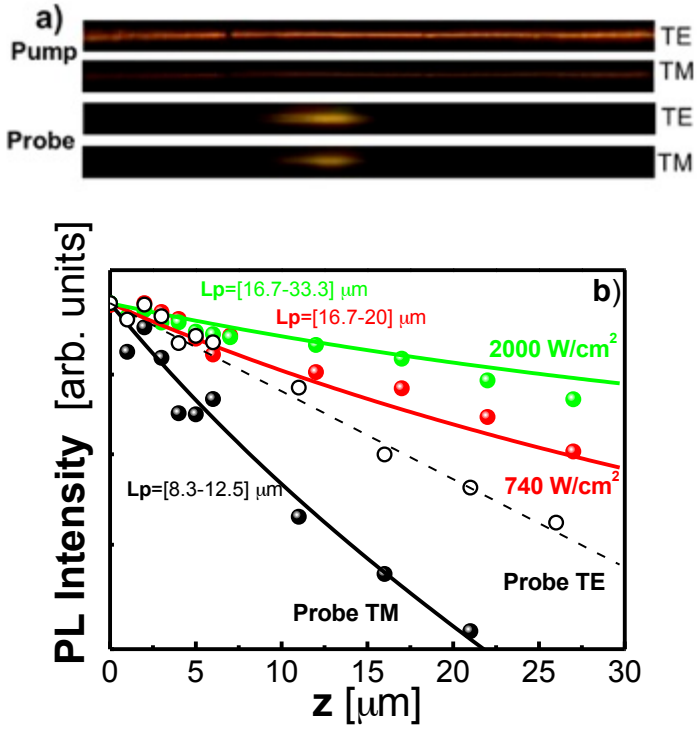


**Figure 21.** Characterization with fiber tip and losses compensation in a sample with the structure shown in Figure 5c at 0.6 μm: a) Near field images by coupling a 405 nm laser at the input edge of the waveguide (top images) and PL excitation at 532 nm by the fiber tip, b) PL intensity as a function of the distance between the tip and the edge of the sample in TM (black solid symbols), TE (black open symbols), and TM with added laser pumping at 405 nm from the edge (red and green data). The curves stand for the fitted single exponential decays.

Plasmonic waveguides with the structure shown in Figure 5d were also characterized by pumping at 532 nm the PL of CdSe QDs with the fiber tip probe and analyzing the waveguided PL signal at the nearest edge of the sample. This design consisted of a *t=30 nm* Au stripe (with widths between 6 and 20 μm) covered by *d=1 μm* of CdSe-PMMA nanocomposite. Due to the small diameter of the tip a pump spot with a FWHM smaller than 10 μm can be obtained on the top of the sample exciting mainly the nanostructures on the stripe. However, part of the beam is spread out of the metal exciting also the dielectric waveguides on the left and on the right of the Au. Figure 22a shows the near field characterization in both polarizations. Clearly light distribution is different out and into the Au stripe. Modes out of the stripe have negligible difference between both polarizations, but light distribution differs completely into the metal. This is due to the fact that the modes in the QD-PMMA dielectric waveguides are purely photonic without strong dependence with polarization; while into the stripe TM modes have plasmonic nature. Since the structures were designed to be single mode, light measured will correspond to PL coupled the LR-SPP in TM polarization and to the $TE_0$ in TE polarization. Propagation length of the structures was also measured by recording the PL signal as a function of the distance between the tip and the edge of the sample. Figure 22b shows the PL signal intensity obtained as a function of the distance between the fiber tip and the waveguide edge for TE and TM polarizations (blue

and red solid symbols, respectively). These curves can be fitted (continuous lines) by the sum of two exponential decays where propagation lengths (LP) of the modes are deduced:

$$I_{PL} = A_1 \cdot e^{-z/Lp_1} + A_2 \cdot e^{-z/Lp_2} \quad (8)$$

where $A_1$ and $A_2$ are constants and $Lp_1$ and $Lp_2$ the propagation length of the modes in the region 1 and 2 respectively (see Figure 22b). The shortest propagation length, $Lp_1$, for the TM mode corresponds to the LR-SPP and can be fitted in the range $Lp_1 = 10 - 16.7\ \mu m$, which again agrees to the calculated value of the LR-SPP (11.4 μm). The fit for the TE mode gives a longer propagation length ($Lp_1=40 - 66.7\ \mu m$), given that this mode is centered at the dielectrics (QD-PMMA nanocomposite) and not at the metal (see inset in Figure 2b). The longest propagation length, $Lp_2$, is around 370 μm and corresponds to the light travelling out of the metal stripe with a negligible dependence with the polarization. The images at the inset of Fig. 22b compares the near field characterization at $z=0$ and $z=250\ \mu m$ at both polarizations. Clearly at $z=0$, plasmonic and photonic modes are present, but for long waveguide lengths ($z=250\ \mu m$) the LR-SPP is lost, i.e., the $TE_0$ on the Au is mostly attenuated and just the photonic modes travelling along the dielectric waveguides are preserved in the structure. The enhancement of Lp for the LR-SPP in the metal can be observed by introducing a pump beam (405 nm CW laser diode) along the dielectric waveguides. Figure 22c compares the PL intensity in TM polarization as a function of the distance between the tip and the edge of the sample without pumping (black) and with two different pump powers (740 W/cm$^2$ in red and 2000 W/cm$^2$ in green). Data without a pump beam was fitted by using equation (2) with $Lp_1=11-16.7\ \mu m$ and $Lp_2=370\ \mu m$. When the pump beam is coupled in the dielectric waveguides the propagation is enhanced. For a pump power of 740 W/cm$^2$ a $Lp_1$ is found in the range $14.3-20\ \mu m$, and for a pump power of 2000 W/cm2 $Lp_1$ was obtained between $14.3-25\ \mu m$.

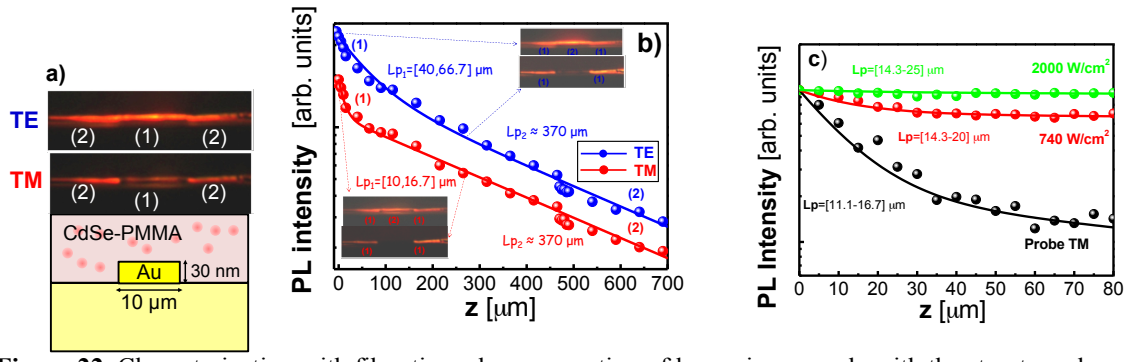


**Figure 22.** Characterization with fiber tip and compensation of losses in a sample with the structure shown in Figure 5d at 0.6 μm. a) Near field images by using the fiber tip excitation (532 nm). b) PL intensity as a function of the distance between the tip and the edge of the sample under TM (red) and TE (blue) polarizations. c) PL intensity as a function of the distance between the tip and the edge of the sample in TM with only the probe (black data) and 740 (red) and 2000 W/cm$^2$ (green) of laser pumping at 405 nm.

### d.2. HgTe-PMMA-emission 1550 nm

The un-optimized HgTe QD material was used to corroborate the enhancement of $L_p$ in plasmonic waveguides at infrared wavelengths, even if in this range we have the limitation of a worse signal-to-noise ratio (by the use of an InGaAs photodiode array instead of a Si CCD). Plasmonic waveguides were cladded by PMMA and the HgTe-PMMA nanocomposite by using the design shown in Figure 5e (with only the bottom PMMA film to prevent metal roughness). Figure 23 shows the fiber-tip characterization in a sample with $ff=0.008$, a

concentration sufficiently low to consider that the structure is symmetric from the point of view of the dielectric constant, and hence the waveguide can support long and short range (LR- and SR-) SPP and $TE_0$ modes; higher order photonic modes are not allowed for the thicknesses considered ($d_1 = 2\ \mu m$, $d_2 = 0$ and $d_3 = 2\ \mu m$). The TM signal shows an intensity distribution centered at the metal, and suffers a higher attenuation, as compared to TE (Fig. 23a). On the other hand, TM signal exhibits two decays (red data in Fig. 23b), the fast one (Lp ≈ 20 μm) attributed to the SR-SPP mode and the slow one (Lp ≈ 200 μm) associated to the LR-SPP. These experimental values are not far from the ones obtained in the simulations: 11.4 and 900 μm for the SR-SPP and LR-SPP modes, respectively. The shorter experimental value of Lp for the LR-SPP as compared to the simulations is associated to roughness in the nanocomposite. For this waveguide any Lp enhancement of the SPP modes was observed after the end-fire coupling of a laser beam for QD pumping, possibly due to the low *ff* used. In this way a second sample was fabricated with a similar structure, but higher QD concentration, *ff* = 0.08. However, for such a high QD concentration the symmetry of the refractive index above/below the gold layer is now broken and the LR-SPP cannot longer exist. The TM signal has a clearly different intensity distribution and a larger attenuation as compared to that of TE (Fig. 24a). The dependence of the guided TM-light as a function of the distance tip-edge also exhibits a double exponential decay (black data in Fig. 4.7b), characterized by Lp(1) ≈ 18 μm, associated to the SR-SPP, and Lp(2) ≈ 67 μm that we attribute to the hybrid photonic-plasmonic mode shown in Fig. 10a. After coupling a pump beam to the input edge of the sample the value of Lp for both modes is enhanced by a 15 % (red curve of Fig. 4.7b), approximately.

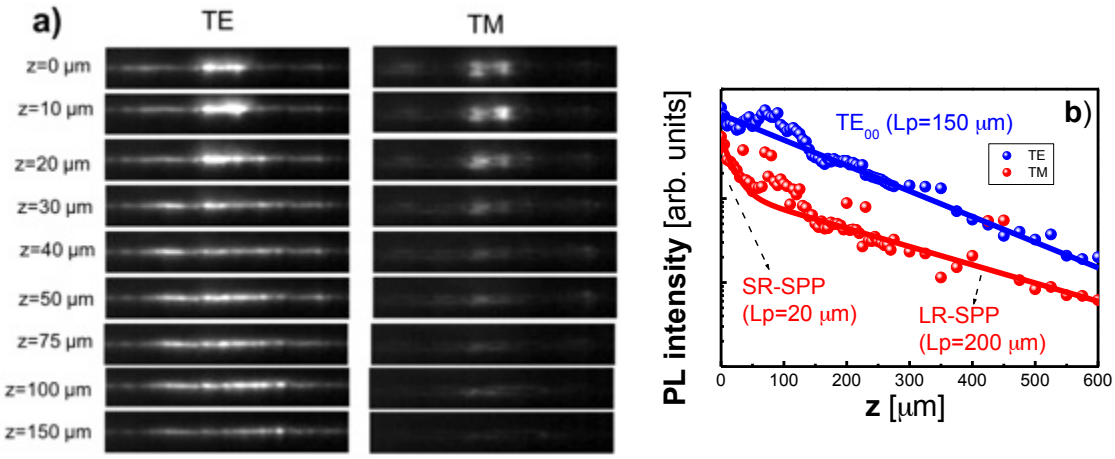


**Figure 23.** Near field images (a) and detected signal as a function of the fiber tip to edge distance at 1.55 μm in the sample described in the text (*ff* = 0.008).

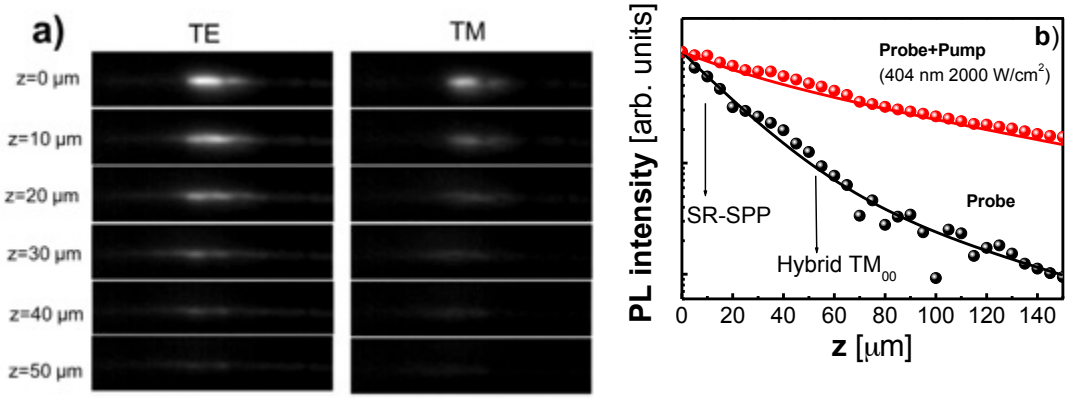


**Figure 24.** Near field images (a) and detected signal as a function of the fiber tip to edge distance at 1.55 μm without (black) / with (red) optical pumping of QDs (b) in the sample described in the text (*ff* = 0.08).

# 4 SiN with embedded QDOTs

## *4.1 Introduction*

Silicon nitride (SiN) exhibits transparency from visible to the infrared wavelength range and has a fairly high optical index (~2.0), enabling its suitability for various photonic applications including integrated photonics [19-20], nonlinear optics [21], and cavity quantum electrodynamics [22]. Here we show that SiN waveguides can be be integrated with colloidal QDs and in that way evolve to an active platform. We will use these hybrid SiN-QD waveguides as the basis for realizing an integrated QD-amplifier. Below we describe how we developed a low-temperature (120-270°) SiN platform. We then fabricated waveguides with a close-packed monolayer colloidal QDs embedded into two layers of SiN, of which the top layer SiN was deposited at 120° to preserve the luminescence ability of QDs maximally. A loss as low as 2.7dB/cm at 900nm wavelength in these hybrid waveguides is demonstrated. The present developed SiN-QDs compatible platform can form the basis for building a hybrid QD-based amplifier.

## *4.2 Mask Design and Fabrication*

Since for the moment optical lithography is utilized to define our waveguide patterns, we designed a contact mask with various waveguide widths from 0.8μm to 2.0μm, each width having a straight reference waveguide and spiral waveguides with different lengths of 1, 2, 4, 8cm. The bend radius of the spiral waveguides is fixed at 100μm and thus the bending loss is negligible according to numerical simulations. Apart from the spiral part, both sides of the waveguide are tapered to 3.0μm for cleaving a facet in measurement. The fabrication includes substrate preparation and waveguide definition, as shown in process flow in Fig. 24(a-e). Firstly we prepare a SiN-QDs-SiN sandwich substrate starting with a silicon wafer with a 3μm thermal $SiO_2$ box layer, onto which a first ~100nm SiN layer is deposited using a low-frequency PECVD process at 270°. Next a close-packed monolayer of colloidal QDs is transferred onto the SiN substrate by a Langmuir–Blodgett (LB) method, as shown in Fig. 24(b). Here we use CdSe/CdS core/shell QDs, a typical visible-emission colloidal QDs, with a diameter of ~7.2nm and a central emission peak of ~620nm. The quality of the QDs film was examined by scanning electron microscope (SEM) and photoluminescence under a UV lamp, as presented in Fig. 24(f) and (g), implying a uniform layer of QDs over large area. A second

~100nm SiN layer is subsequently deposited for embedding of the LB QDs layer, and this time the deposition temperature is lowered to 120° thus to reduce the possible degradation of the optical quality of the QDs for luminescence [23], while still to retain the material quality of SiN for low-loss photonics. Actually, as measured by ellipsometry, the refractive index of SiN at 900nm changes from 1.92 to 1.85 with the temperature decreasing from 270° to 120°. After preparation of the substrate, the photoresist mask for waveguide is patterned using contact lithography, and the resist process is also optimized to have a steep and smooth sidewall that is critical for dry etching. Finally, the waveguide pattern is transferred onto the SiN substrate using reactive ion etching (RIE) process. We also fabricated the waveguides with two layers of SiN-SiN film deposited at 270° and 120°, respectively, so as to compare the difference of etching and waveguide loss.

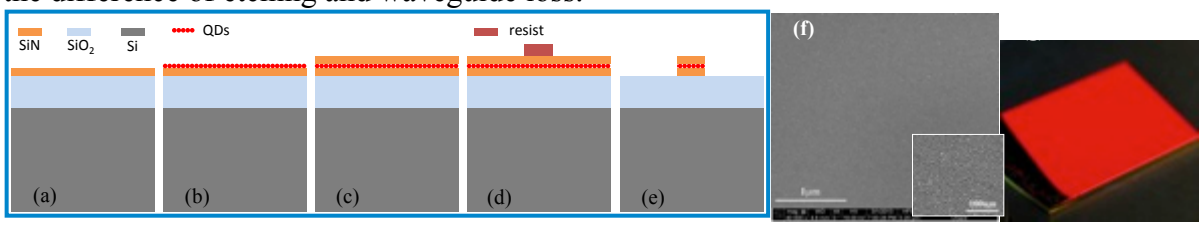


**Fig. 24 (a-e) Schematics of SiN-QDs-SiN hybrid waveguide fabrication flow. (f) SEM image of the LB QDs film and (g) photoluminescence of a 2cm×2cm monolayer of QDs.**

The optimization of RIE conditions is needed for the realization of vertical and smooth sidewalls and thereby for the achievement of low-loss waveguides. Since the material density and therefore the etch behavior for SiN deposited at different temperature vary a lot, the etching should be a sufficiently anisotropic process with adequate protection for the sidewall, thus to realize a topologically united side surface without obvious step. Furthermore, regarding the particular etching of SiN-QDs-SiN, this RIE process should also be capable of etching through QDs and ensuring the continuity of etching. In our investigation, we employed $CF_4/H_2$ gases for both SiN-SiN and SiN-QDs-SiN etching, and all the plasma conditions such as gas ratio, RIE power and chamber pressure were systematically optimized to obtain a vertically etched profile and smooth surface, by using focused ion beam (FIB) milled cross section and SEM analysis. In order to avoid charging effects caused by the nonconductive nature of SiN and $SiO_2$ and to acquire improved images, we carried out the etching and the corresponding SEM check on the bare silicon substrate without $SiO_2$ box layer, and in this way we could inspect both the etched profile and the surface roughness. Fig. 25(a) and (b) show the FIB cross section and the sidewall images of the etched SiN-SiN film with remained resist mask, and it can be seen that the etching is almost vertical and there is no observable step at the interface of two layers of SiN. Besides, from Fig. 25(b) the sidewall exhibits much smooth surface without distinct roughness. In Fig. 25(c) and (d), we show the associated images of the etched SiN-QDs-SiN film, and the etched profile presents slightly positive slope with visible sidewall roughness, by comparing with SiN-SiN, due to the even large material quality difference between the SiN on a flat substrate and the one on a QDs surface. The interface of SiN-QDs can also be seen in Fig. 25(c) and (d), which indicates that the monolayer of QDs is well embedded in the SiN matrix.

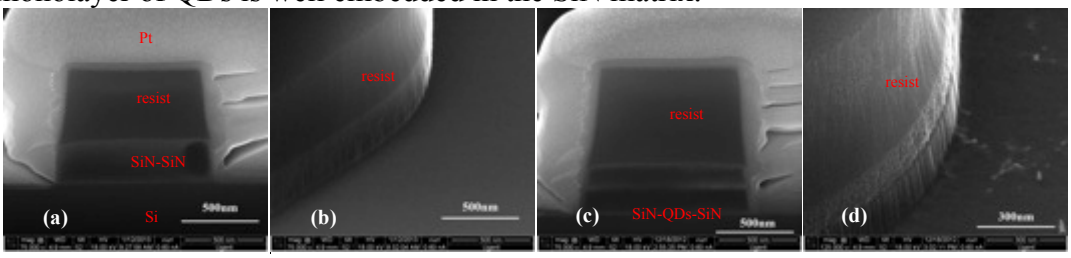

**Fig. 25. (a) FIB cross section and (b) sidewall images of the etched two layers of SiN-SiN prepared at 270° and 120°, respectively. (c) FIB cross section and (d) sidewall images of the etched SiN-QDs-SiN sandwich film.**

## *4.3 Loss Measurement and Discussion*

Propagation loss was measured with the cut-back method by using spiral waveguides with different lengths, and the loss was extracted by fitting the length-dependent fiber-to-fiber transmission. The measurement was done by using a near-infrared tunable laser on a horizontal setup with microlensed fibers coupled in and out to the cleaved facets of the waveguide. The transmitted power is maximized with a polarizer and the measured loss is believed to represent the TE modes instead of higher-loss TM modes. As mentioned before, the target of this work is to develop and demonstrate a SiN-QDs compatible technical platform with low-loss passive photonics and efficient photon emitters inside, and the fabrication issues especially the deposition and etching for this hybrid structure will be primarily concerned. As a consequence, we measured the waveguide loss at 900nm wavelength in order to eliminate the intrinsic absorption contributed by QDs layer. In Fig. 26(a), we plot the waveguide loss as a function of the nominal width on the mask for both SiN-SiN and SiN-QDs-SiN films, where a total ~200nm thick SiN was deposited. For both cases, the loss gradually decreases when widening the width from 0.8μm to 1.5μm, and when further increasing the width to 2.0μm the loss reaches to saturated values of 1.7dB/cm and 2.7dB/cm for SiN-SiN and SiN-QDs-SiN systems, respectively. It is also clear that the SiN-QDs-SiN waveguide has higher loss than that in SiN-SiN over all widths, which can be attributed to the presence of the more surface roughness of the etched sidewalls in SiN-QDs-SiN as shown is Fig. 25(d), leading to increased scattering loss. In Fig. 26(b) and (c), we present the FIB cross-section images of 2.0μm-wide waveguide for SiN-SiN and SiN-QDs-SiN films, respectively. Again we observe a slightly tilted etched profile compared to the vertical sidewall in SiN-SiN, which possibly results in additional loss in SiN-QDs-SiN waveguide. According to calculation, the upper cut-off width for TE singlemode SiN waveguide with 200nm thickness at 900nm wavelength is around 1.2μm, and for 2.0μm width the waveguide is certainly multimode in which the sidewall roughness becomes less important, while the roughness at interfaces between different layers will be responsible for the waveguide loss (without considering material loss). In SiN-QDs-SiN system, the LB QDs surface is assumed to be rougher than deposited SiN surface, due to the size dispersion of QDs and the imperfections in the LB film. Therefore, the scattering loss at QDs-SiN and top SiN interfaces increase significantly, which could account for the remained 1dB/cm loss difference at 2.0μm width between SiN-SiN and SiN-QDs-SiN waveguides. Note that due to the limitation of contact optical lithography the width variation along the waveguide will increase notably when reducing the pattern width, which can also introduce extra loss.

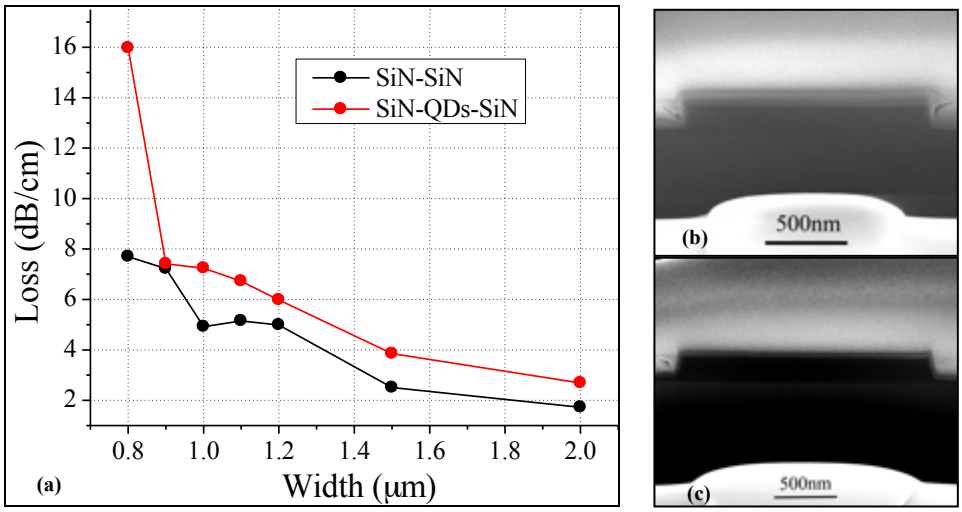


**Fig. 26. (a) Measured loss for different waveguide widths. The FIB cross-section images of 2μm-wide waveguide for (b) SiN-SiN and (c) SiN-QDs-SiN films, respectively.**

## *4.4 Towards electrical injection*

To verify the electrical injection with the optimized low temperature SiN-process, we prepared new QD-dielectric stacks, which can be driven by applying an AC-voltage over the stack [24]. As demonstrated earlier, applying a voltage over the QD-stack leads to exiton formation in the center of the stack, leading to light emission. By alternating the voltage, this light generation can be maintained. Our earlier stacks were built up using ALD-deposited AlOx layers. The ALD-process leads to very dense layers, resistant to the high voltage. It was however not a priori clear that the low temperature SiN-layers described above do not exhibit pinholes and can withstand the high voltage needed. Therefore we fabricated a number of test stacks consisting of an ITO substrate (on glass), SiN bottom layer (50nm), CdSe/CdS QDOT-layer (26nm, 44nm, 66nm), a low temperature SiN top layer (50nm) and an Aluminum top contact (Fig. 27).

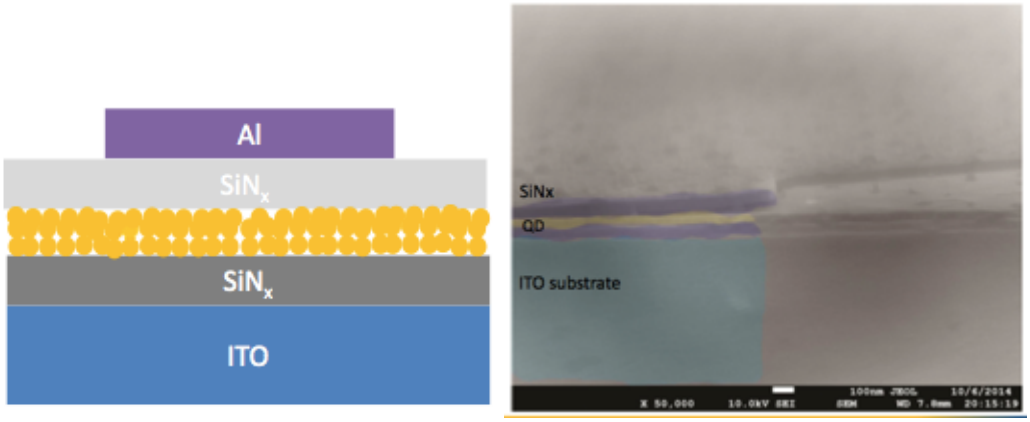


**Fig. 27 (a) Schematic cross-section of the AC-stack for electrical injection. (b) SEM-picture of cross-section.**

These stacks where then tested by applying a high AC voltage (up to 150V). Delamination of the metal contact has been seen but the SiN layer was demonstrated to be of sufficient high quality for building further devices. Fig. 28 a) shows a picture of the emitted light (note that we choose visible QDs here for easier characterization) and Fig. 28 b) shows the spectral characteristics under optical (PL) and electrical (EL) pumping.

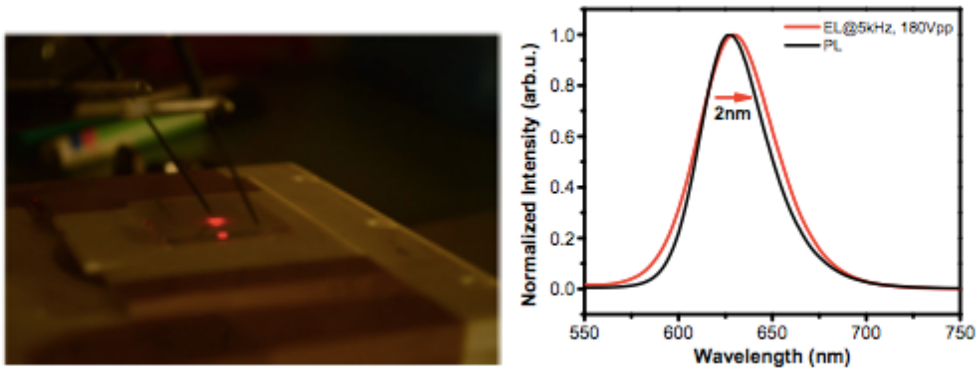


**Fig. 28 (a) Photograph of electrically injected QD-stack. (b) Electroluminescence and Photoluminescence spectrum of stack shown in Fig. 27.**

Fig. 29 shows how the output power and central wavelength change as function of applied voltage and AC-frequency, with the latter currently limited by the large capacitance of the device. These results show the high quality of the SiN-layers and the deposited stacks. They will form the basis for further integration.

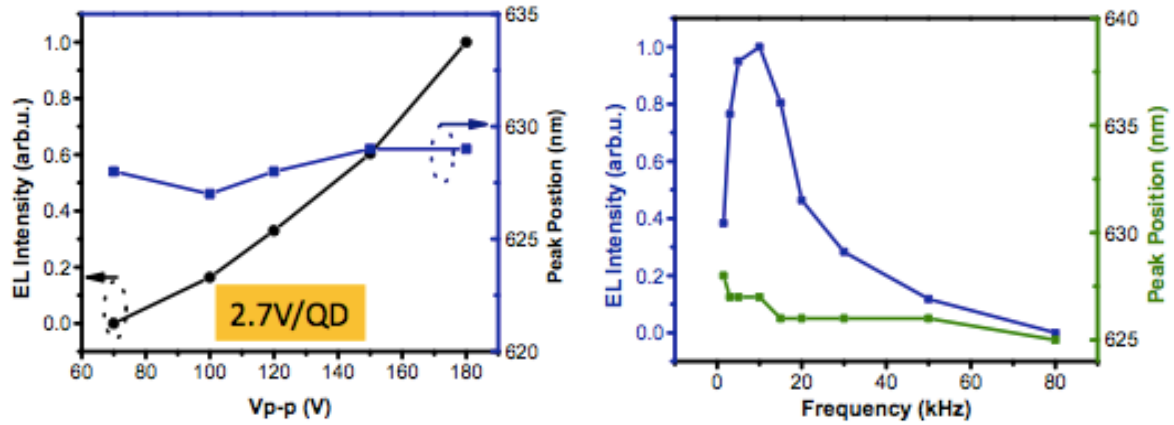


**Fig. 29 Output power and peak wavelength as function of applied voltage (a) and AC frequency (b)**

# 5 Conclusions

The most important conclusions regarding the work developed until the moment on plasmonic amplifiers are:

(1) We have designed and fabricated different promising designs towards achieving plasmonic amplification (propagation length compensation) provided a QD material with net gain.

(2) We have been working with different QD materials, some of them exhibiting gain at sufficiently high incident (pulsed) laser power in colloidal state, but, except for HgTe, net gain is not observed when QDs are deposited in the form of dense films or embedded in polymers. The most promising QD material is therefore HgTe.

(3) An experimental method has been developed to extract the propagation length of the Surface Plasmon Polariton propagating on metal waveguides. This magnitude seems to be partially compensated when the QD-polymer nanocomposites are optically pumped, even if they are not exhibiting net gain.

(4) A powerfull SiN waveguide platform has been developed that is also compatible with electrical AC-injection. This platform will form the basis for further integration.

# 6 References

[1] D.K. Gramotnev and S.I. Bozhevolnyi, "Plasmonics beyond the diffraction limit", *Nature Photonics*, **4**, 83-91 (2010)
[2] J. Leuthold et al., "Plasmonic Communicatinos. Light on a wire", *Optics and Photonics News*, 30 (2013)
[3] P. Berini and I. De Leon, "Surface plasmon-polariton amplifiers and lasers", *Nature Photonics*, **6**, 16-24 (2012)
[4] R.F. Oulton et al., "A hybrid plasmonic waveguide for subwavelength confinement and long-range propagation", *Nature Photonics*, **2**, 496-500 (2008)
[5] P. Berini, "Long-range surface plasmon polaritons", *Advances in Optics and Photonics*, **1**, 484-588 (2009)
[6] I. De Leon and P. Berini, "Amplification of long-range surface plasmons by a dipolar gain medium", *Nature Photonics*, **4**, 382-387 (2010)
[7] M.C. Gather et al., "Net optical gain in a plasmonic waveguide embedded in a fluorescent polymer", *Nature Photonics*, **4**, 457-461 (2010)
[8] M. Ambati et al., "Observation of stimulated emission of surface plasmon polaritons", *Nanoletters*, 8, 3998-4001 (2008)
[9] J. Grandidier et al., "Gain-assisted propagation in a plasmonic waveguide at telecom wavelength", *Nanoletters*, **9**, 2935-2939 (2009)
[10] I. Suárez et al., "Photoluminiscence waveguiding in CdSe and CdTe QDs-PMMA nanocomposite films", *Nanotechnology*, **22**, 435202 (2011)
[11] H. Gordillo et al., "Polymer/QDs nanocomposite for waveguiding applications" *Journal of Nanomaterials*, **2012**, 960201 (2012)
[12] I. Suárez et al. "Designs of plasmonics amplifiers" Navolchi Deliverable 4.1
[13] I. Suárez et al. "Report on optical properties of QDs layers and polymer nanocomposites" Navolchi Deliverable 4.2
[14] G. Lifante, "Integrated Photonics. Fundamentals", ed. John Wiley & Sons, 2003.
[15] P. Berini, "Long-range surface plasmon polaritons", *Advances in Optics and Photonics*, **1**, 484-588 (2009)
[16] V. I. Klimov, "Nanocrystal quantum dots: from fundamental photophysics to multicolor lasing", *Los Alamos Science*, **28**, 214-220 (2003).
[17] H. Gordillo I. Suárez, R. Abargues, P. Rodríguez-Cantó and J.P. Martínez-Pastor, " Color tuning and white light by dispersing CdSe, CdTe and CdS in PMMA nanocomposite waveguides", *IEEE Photonics Journal*, **5**, 2201412 (2013)
[18] H. Gordillo I. Suárez, R. Abargues, P. Rodríguez-Cantó, G. Almuneau and J.P. Martínez-Pastor, "Quantum-dot double layer polymer waveguides by evanescent light coupling" *IEEE Journal of Lightwave Technology*, **31**, 2515-2525 (2013)
[19] Q. Li, A. A. Eftekhar, M. Sodagar, Z. X. Xia, A. H. Atabaki, and A. Adibi, "Vertical integration of high-Q silicon nitride microresonators into silicon-on-insulator platform," Opt Express 21, 18236-18248 (2013).
[20] A. Z. Subramanian, P. Neutens, A. Dhakal, R. Jansen, T. Claes, X. Rottenberg, F. Peyskens, S. Selvaraja, P. Helin, B. Du Bois, K. Leyssens, S. Severi, P. Deshpande, R. Baets, and P. Van Dorpe, "Low-Loss Singlemode PECVD Silicon Nitride Photonic Wire Waveguides for 532-900 nm Wavelength Window Fabricated Within a CMOS Pilot Line," IEEE Photonics J 5 (2013).

[21] D. J. Moss, R. Morandotti, A. L. Gaeta, and M. Lipson, "New CMOS-compatible platforms based on silicon nitride and Hydex for nonlinear optics," Nat Photonics 7, 597-607 (2013).
[22] M. W. McCutcheon, and M. Loncar, "Design of a silicon nitride photonic crystal nanocavity with a Quality factor of one million for coupling to a diamond nanocrystal," Opt Express 16, 19136-19145 (2008).
[23] B. De Geyter, K. Komorowska, E. Brainis, P. Emplit, P. Geiregat, A. Hassinen, Z. Hens, and D. Van Thourhout, "From fabrication to mode mapping in silicon nitride microdisks with embedded colloidal quantum dots," Appl Phys Lett 101 (2012).
[24] V. Wood, J. Halpert, and M. Panzer, “Alternating Current Driven Electroluminescence from ZnSe / ZnS : Mn / ZnS Nanocrystals,” Nano Lett., 2009.